J. Fluid Mech. (2002), *vol.* 452, *pp.* 263–291. © 2002 Cambridge University Press
DOI: 10.1017/S0022112001006711 Printed in the United Kingdom

A super-rotating shear layer in magnetohydrodynamic spherical Couette flow

By E. DORMY[1], D. JAULT[2] AND A. M. SOWARD[3]

[1]Institut de Physique du Globe de Paris/CNRS, 4 place Jussieu, 75252 Paris Cedex 05, France
[2]LGIT/CNRS, Université Joseph Fourier BP53, 38041 Grenoble Cedex 9, France
[3]School of Mathematical Sciences, University of Exeter, Exeter EX4 4QE, UK

(Received 19 February 2001 and in revised form 12 July 2001)

We consider axisymmetric magnetohydrodynamic motion in a spherical shell driven by rotating the inner boundary relative to the stationary outer boundary – spherical Couette flow. The inner solid sphere is rigid with the same electrical conductivity as the surrounding fluid; the outer rigid boundary is an insulator. A force-free dipole magnetic field is maintained by a dipole source at the centre. For strong imposed fields (as measured by the Hartmann number M), the numerical simulations of Dormy *et al.* (1998) showed that a super-rotating shear layer (with angular velocity about 50% above the angular velocity of the inner core) is attached to the magnetic field line $\mathscr{C}$ tangent to the outer boundary at the equatorial plane of symmetry. At large M, we obtain analytically the mainstream solution valid outside all boundary layers by application of Hartmann jump conditions across the inner- and outer-sphere boundary layers. We formulate the large-M boundary layer problem for the free shear layer of width $M^{-1/2}$ containing $\mathscr{C}$ and solve it numerically. The super-rotation can be understood in terms of the nature of the meridional electric current flow in the shear layer, which is fed by the outer-sphere Hartmann layer. Importantly, a large fraction of the current entering the shear layer is tightly focused and effectively released from a point source at the equator triggered by the tangency of the $\mathscr{C}$-line. The current injected by the source follows the $\mathscr{C}$-line closely but spreads laterally due to diffusion. In consequence, a strong azimuthal Lorentz force is produced, which takes opposite signs either side of the $\mathscr{C}$-line; order-unity super-rotation results on the equatorial side. In fact, the point source is the small equatorial Hartmann layer of radial width $M^{-2/3}$ ($\ll M^{-1/2}$) and latitudinal extent $M^{-1/3}$. We construct its analytic solution and so determine an inward displacement width $O(M^{-2/3})$ of the free shear layer. We compare our numerical solution of the free shear layer problem with our numerical solution of the full governing equations for M in excess of 10^4. We obtain excellent agreement. Some of our more testing comparisons are significantly improved by incorporating the shear layer displacement caused by the equatorial Hartmann layer.

1. Introduction

The steady flow of viscous fluid confined inside a spherical shell, which results when the inner (radius r_i^*) and outer (radius r_o^*) boundaries rotate at different angular velocities Ω_i^* and Ω_o^* respectively about a common axis, is referred to as spherical Couette flow. When the spheres almost corotate rapidly, the motion measured in a frame corotating with (say) the outer sphere is slow and satisfies linear equations. The determination of the resulting steady flow is a classical problem in the theory of

https://doi.org/10.1017/S0022112001006711 Published online by Cambridge University Press

rotating fluids. Proudman (1956) showed that the mainstream flow outside boundary layers is predominantly geostrophic, while its magnitude is determined by the Ekman suction into and out of the Ekman layers attached to the inner and outer spherical boundaries. The Ekman layer is singular on the equator of the inner sphere; this feature is linked to the existence of a free shear layer on the tangent cylinder to the inner sphere extending from its equator to the intersection with the outer sphere. The nature of the flow in this tangent-cylinder shear layer was resolved by Stewartson (1966), while the extension of this shear layer analysis to more general geometries was undertaken by Moore & Saffman (1969). The strong shear at the tangent cylinder was reproduced numerically by Hollerbach (1994) down to small Ekman number $E = 5 \times 10^{-6}$. Decreasing E further to $E = 10^{-8}$, Dormy, Cardin & Jault (1998) recovered the structure of the free shear layer found by Stewartson (1966).

In the case of electrically conducting fluid, the magnetohydrodynamic flow that results in the presence of an applied axisymmetric meridional (poloidal) magnetic field is considerably more complicated. The MHD extension to the Proudman–Stewartson problem described above was first investigated numerically by Hollerbach (1994), who considered an axial dipole magnetic field. The inner solid sphere ($r^* \leqslant r_i^*$) was assumed to be an insulator (unlike the case of a solid sphere with the same electrical conductivity as the fluid, which we will consider) as was the solid outer region ($r^* \geqslant r_o^*$). When the applied dipole magnetic field is sufficiently weak that the Lorentz force, as measured by the Hartmann number M, remains small compared to the Coriolis force (specifically small Elsasser number EM^2), he found that a free shear layer remained on the tangent cylinder; the structure of this layer was determined by Kleeorin *et al.* (1997). When the Coriolis and Lorentz forces are comparable, $EM^2 = O(1)$, the inner and outer boundary layers are of mixed Ekman–Hartmann type, whereas the free shear layer evaporates. Nevertheless, when the applied magnetic field is strong, $EM^2 \gg 1$, a free shear layer reappears but now aligned with the magnetic field lines which graze either the inner or the outer boundary; elsewhere on these boundaries the boundary layers are predominantly Hartmann in character. Models of this type were developed by Starchenko (1997). In the case of the dipole field, the grazing field line is the one which touches the outer spherical boundary at its equator. The strong dipole field is the limit that interests us here and below we will expand in greater detail on the background to our chosen model.

The rapid rotation limit $E \ll 1$ with $EM^2 = O(1)$ has geophysical applications. The numerical geodynamo simulations of Glatzmaier & Roberts (1995) have revealed the importance of detached shear layers in rotating MHD systems. Indeed a liquid sodium prototype of a dynamo experiment based on fluid instabilities riding on these layers is now being built in Grenoble: a spherical cavity filled with sodium will be enclosed between a permanent magnet and an outer container made of inox; measurement of the electrical potential will give insight into the dynamics inside the cavity because the outer boundary is poorly conducting. Recently there has been much discussion about a possible differential rotation between the solid inner core and the mantle of the Earth. There is now some evidence indicating that the speed of the inner core surface relative to the mantle is no larger than the fluid velocity at the core surface, as inferred from the secular variation of the Earth's magnetic field (Vidale, Dodge & Earle 2000). The differential rotation between the inner solid core and the outer solid mantle, together with the detached shear layers occurring in the numerical dynamo experiments, points to the importance of the idealized model of spherical Couette flow in the presence of an applied magnetic field, as described above. Kleeorin *et al.* (1997) adopted an applied dipole field because it is meridional and as such interacts

https://doi.org/10.1017/S0022112001006711 Published online by Cambridge University Press

strongly with the predominantly azimuthal flow driven by the differential rotation of the boundaries. Another attractive feature of a dipole magnetic field is that it is force free and so by itself drives no motion. Of course, in the Earth that differential rotation may well be caused by the angular momentum transport resulting from asymmetric convection; such complications are outside the scope of the simplified models driven by differential rotation described above.

In order to understand processes that are predominantly magnetic in character, we concern ourselves with the strong field limit $EM^2 \gg 1$. This is outside the geophysically relevant parameter range, but may be pertinent to certain slowly rotating planetary objects with strong magnetic fields. Then the Coriolis force is relatively small and whether or not the system is in rapid rotation ceases to be a significant issue (Starchenko 1997). Much of the dynamics in that limit is captured by the simpler problem in which the outer sphere is at rest ($\Omega_o^* = 0$). We will study that problem in the case of small differential rotation and so will require that the inner sphere rotates slowly. Motivated by planetary applications, we assume that the inner sphere is electrically conducting having the same conductivity as the fluid, while the outer boundary is an electrical insulator. Though, of course, for laboratory applications other electrical boundary conditions are of interest too. The typical strength B_0^* of the force-free applied dipole magnetic field and the importance of advection are measured by the Hartmann and magnetic Reynolds numbers

$$M = \frac{L^* B_0^*}{\sqrt{\mu_o \rho \nu \eta}} \quad \text{and} \quad R_M = \frac{L^{*2} \Omega_i^*}{\eta} \quad (L^* = r_o^* - r_i^*) \tag{1.1a,b}$$

respectively, where ρ is the density, ν is the viscosity, μ_o is the magnetic permeability and η is the magnetic diffusivity. We restrict attention to strong magnetic fields and slow steady flow which correspond to the limits

$$M \gg 1 \quad \text{and} \quad R_M \ll 1. \tag{1.2a,b}$$

The later assumption ensures that the magnetic field perturbations are small and is essentially the basis on which we linearize our equations.

In our large Hartmann number limit, various boundary layers can be isolated. Hartmann layers of width $\delta_H^* = \sqrt{\mu_0 \rho \nu \eta}/B_0^* = L^*/M$ form on the inner and outer boundaries. The free shear layer, mentioned above, forms about the magnetic field line, which we call $\mathscr{C}$, that touches the outer sphere at its equator. This layer has characteristics similar to the free shear layer caused by current injection and removal by electrodes in channel flow (see Müller & Bühler 2001, Chap. 7) and has the same width $\sqrt{L^* \delta_H^*} = L^*/M^{1/2}$ as sidewall boundary layers (see Roberts 1967*a*). The presence of the $\mathscr{C}$-line shear layers in the shell were clearly identified by the numerical simulations of Dormy *et al.* (1998) (see also Dormy 1997 and the discussion in Starchenko 1998*a*,*b*). Surprisingly Dormy *et al.* (1998) found that the angular velocity in these $M^{-1/2}$-shear layers exceeded by about 50% the angular velocity Ω_i^* of the inner sphere. We say surprising because Lenz's law says that the Lorentz force acts to retard motion, which locally is evidently not true here. Indeed the situation provides yet another 'warning example to those who might wish to apply Lenz's law in detail!' (Roberts 1967*a*, p. 183). Dormy *et al.*'s (1998) finding was subsequently given further numerical support by Hollerbach (2000, 2001) and Hollerbach & Skinner (2001). Those papers emphasize that the nature of the electromagnetic boundary conditions play an extremely important role. Indeed their numerical results show that when both the inner and outer spheres are electrically conducting, the super-rotation is very large, $O(M^{0.6})$. The sensitivity to boundary conditions can be traced to the role played

https://doi.org/10.1017/S0022112001006711 Published online by Cambridge University Press

by the Hartmann jump conditions on the inner and outer boundaries. We elaborate on this point in § 6, where we offer a tentative explanation for this large power law. A comprehensive analysis of that intriguing case is challenging and lies outside the scope of this present paper.

Though Starchenko (1997) considered the case of a rotating shell ($E \ll 1$), he worked in the large Elsasser number limit for which the boundary layer structures that he isolated are largely similar to those that we consider. Indeed, he proposed a mechanism for super-rotation. The effect he isolated is in fact small but may well produce an $O(M^{-1})$ super-rotation in the equatorial mainstream region, as we explain in § 6. Nevertheless, being small it is not responsible for the $O(1)$ super-rotation that occurs in the $\mathscr{C}$-line shear layer.

In this paper, we develop an asymptotic large-M theory and compare it with numerical integrations of the complete governing equations at large but finite M. Our development is organized as follows. In § 2 we formulate our problem. We describe the mainstream solution, first obtained by Starchenko (1997), valid outside boundary layers and compare it to the numerical solution of the complete governing equations. The differential rotation leads to a current flow from the inner conducting sphere out through the fluid along the meridional magnetic field lines. On arrival at the outer boundary it is carried to the equator inside the Hartmann boundary layer and is returned along the $\mathscr{C}$-line to the inner sphere. In § 3.1 we formulate the $\mathscr{C}$-line shear layer problem and report results of its numerical solution; in § 3.2 we obtain analytic solutions for the narrow gap limit. In § 4 more detailed comparisons are made between the numerical results for the boundary layer and the complete problem. Now it is important to appreciate that a significant fraction of the Hartmann layer current reaches the small equatorial Hartmann layer (the shaded region on figure 7 below), which is only a point on the scale of the $\mathscr{C}$-line shear layer. The current from this point source follows the $\mathscr{C}$-line but spreads laterally causing the azimuthally directed Lorentz force to take opposite signs on either side. The fluid is de-accelerated (accelerated) on the polar (equatorial) side by an $O(1)$ amount. The equator-side acceleration provides the $O(1)$ super-rotation.

Some small discrepancies are found in the numerical comparisons between the full numerics and the shear layer theory. These may be traced to low-order corrections which arise because the free shear layer intersects the outer-sphere boundary in the vicinity of its equator over a relatively long latitudinal length $O(L^*M^{-1/4})$. Here a thin Hartmann layer can still be distinguished but thickens as the equator is approached. Eventually it becomes the equatorial Hartmann layer, which constitutes the source mentioned above, with characteristics more in common with sidewall boundary layers; it has width $O(L^*M^{-2/3})$, extends over the latitudinal length scale $O(L^*M^{-1/3})$ and its existence leads to the source of the dominant correction to the free shear layer. In § 5, we obtain the analytic solution for this layer using a remarkable technique developed by Roberts (1967*b*) (see also Roberts 2000) for a closely related problem. Our result enables us to determine a displacement thickness $\delta^* = O(L^*M^{-2/3})$ for the $M^{-1/2}$-shear layer. By that we mean that the shear layer is effectively triggered on the equatorial plane at a radius $r_o^* - \delta^*$ rather than at the outer boundary r_o^*. With the inclusion of this correction to the shear layer solution, we find excellent agreement with the full numerical simulations.

2. Formulation

We adopt L^*, $L^*\Omega_i^*$ and B_0^* as our units of length, velocity and magnetic field respectively; the superscript star is dropped for all dimensionless quantities.

https://doi.org/10.1017/S0022112001006711 Published online by Cambridge University Press

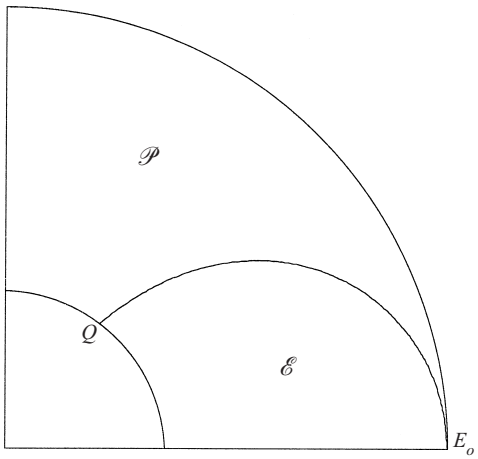


FIGURE 1. The northern hemisphere geometry. At large M, the polar $\mathscr{P}$ and equatorial $\mathscr{E}$ mainstream regions are separated by the shear layer containing the magnetic field line $\mathscr{C}$ joining E_o to Q.

Relative to cylindrical polar coordinates (s, ϕ, z), our applied dipole magnetic field is

$$\boldsymbol{B}_M = \nabla A \times \frac{\hat{\boldsymbol{\phi}}}{s} = -\nabla \Phi = \left(\frac{3sz}{2r^5}, 0, \frac{2z^2 - s^2}{2r^5} \right), \tag{2.1a}$$

where

$$A = \tfrac{1}{2}\, s^2/r^3, \quad \Phi = \tfrac{1}{2}\, z/r^3 \quad \left(r := \sqrt{s^2 + z^2} \right). \tag{2.1b}$$

It determines

$$s^{-2}|\nabla A| = |\boldsymbol{B}_M|^2 = \tfrac{1}{4}\,(s^2 + 4z^2)/r^8. \tag{2.1c}$$

The magnetic field line $\mathscr{C}$: $A = 1/2r_o$ divides the fluid shell up into two domains $\mathscr{P}$: $A < 1/2r_o$ and $\mathscr{E}$: $A > 1/2r_o$. In the former polar domain $\mathscr{P}$ the magnetic field lines intersect both the inner and outer shell boundaries $r = r_i$ and $r = r_o$, where $r_o - r_i = 1$. In the latter equatorial domain $\mathscr{E}$ the magnetic field lines intersecting the inner sphere boundary cross the equator within the fluid and return to the inner sphere without ever meeting the outer spherical boundary. The dividing line $\mathscr{C}$ is important because it has grazing contact with the outer sphere at the equator E_o. There we find it convenient to introduce the alternative Hartmann number

$$\mathscr{M} := \tfrac{1}{2}\, r_o^{-2} M \tag{2.2}$$

based on the local magnetic field strength $B_0^*/2r_o^3$ ($s = r_o$, $z = 0$ in (2.1c)) and the length r_o^*. We denote the intersection of $\mathscr{C}$ with the inner sphere by Q (see figure 1).

The slow steady azimuthal velocity $(0, s\Omega, 0)$ forced by rotating the inner sphere induces small magnetic field perturbations $(0, R_M B, 0)$. The equations of motion and magnetic induction are linearized on the basis that R_M is small and their ϕ-components give

$$M^2 s^{-1}\, \boldsymbol{B}_M \cdot \nabla\,(sB) + \left(\nabla^2 - s^{-2}\right)(s\Omega) = 0, \tag{2.3a}$$

$$s\, \boldsymbol{B}_M \cdot \nabla\, \Omega + \left(\nabla^2 - s^{-2}\right) B = 0. \tag{2.3b}$$

https://doi.org/10.1017/S0022112001006711 Published online by Cambridge University Press

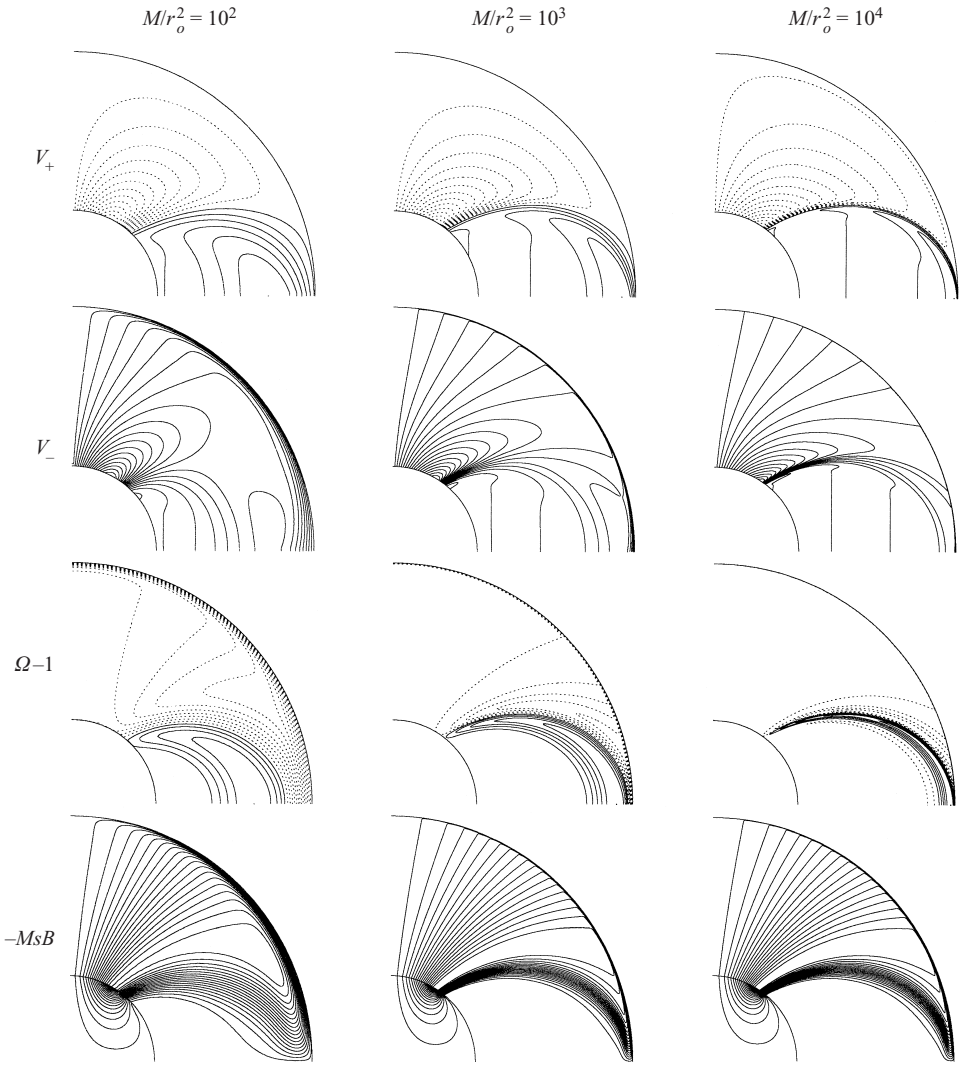


FIGURE 2. The full numerical solutions of the governing equations for the radius ratio $r_i/r_o = 0.35$ at increasing values of M. Contours at uniformly spaced levels of constant positive (negative) isovalues of V_+, V_-, $\Omega - 1$ and $-MsB$ in the meridional plane are indicated by the continuous (dotted) lines.

On the rigid outer insulating boundary ($r = r_o$), we require that

$$\Omega = 0, \quad B = 0, \tag{2.4a,b}$$

while on the inner boundary ($r = r_i$), the no-slip condition requires that

$$\Omega = 1. \tag{2.5a}$$

Since the inner solid sphere is a conductor with the same conductivity as the fluid, we therefore require that

$$B \quad \text{and} \quad \frac{\partial B}{\partial r} \quad \text{are continuous across} \quad r = r_i \tag{2.5b}$$

https://doi.org/10.1017/S0022112001006711 Published online by Cambridge University Press

with B satisfying

$$\left(\nabla^2 - s^{-2}\right) B = 0 \quad \text{in} \quad r < r_i. \tag{2.6}$$

It is also helpful to take advantage of the symmetries corresponding to those of the applied dipole field, $A(s,-z) = A(s,z)$, namely $\Omega(s,-z) = \Omega(s,z)$ and $B(s,-z) = -B(s,-z)$, which respectively imply

$$\frac{\partial \Omega}{\partial z} = B = 0 \quad \text{on the equator} \quad z = 0. \tag{2.7}$$

In the large Hartmann number limit $M \gg 1$ for which our asymptotic analysis is valid, the dissipation in the mainstream exterior to all boundary layers is negligible. With the neglect of viscosity, the Lorentz force vanishes $\boldsymbol{j} \times \boldsymbol{B}_M = \boldsymbol{0}$, where $\boldsymbol{j} = s^{-1}\nabla sB \times \hat{\boldsymbol{\phi}}$ is the electric current measured in appropriate units, implying that the current lines $sB =$ constant are aligned with the meridional magnetic field lines. Likewise with the neglect of Ohmic diffusion, the magnetic field is frozen to the fluid and satisfies Ferraro's (1937) *law of isorotation*, namely that the angular velocity Ω is constant on field lines. From a more formal point of view, (2.3) have solutions with functional form

$$\Omega = \mathscr{F}(A) + O(M^{-1}), \quad sB = -r_o^2 M^{-1} \mathscr{G}(A) + O(M^{-2}) \tag{2.8a,b}$$

(cf. Starchenko 1997, equation (31)), in which the leading-order terms depend on A alone.

In order to understand the nature of the boundary layer structures, we introduce the Alfvén variables

$$V_\pm = s\Omega \pm MB, \tag{2.9}$$

which satisfy (2.3) when

$$\boldsymbol{B}_M \cdot \nabla V_\pm \pm M^{-1}\left(\nabla^2 - s^{-2}\right) V_\pm = s^{-1} B_s V_\mp. \tag{2.10}$$

They should be interpreted as advection–diffusion equations, which are coupled by the source terms on their right-hand sides. The advection is manifested by $\boldsymbol{B}_M$; when $\boldsymbol{B}_M$ directed from the inner to the outer sphere, V_+ (V_-) is convected inwards (outwards). As a consequence, V_+ (V_-) is continuous across the Hartmann layer on the outer (inner) sphere. Continuity of V_+ across the outer Hartmann layer together with the boundary condition (2.4a,b) implies that the mainstream boundary condition on the outer sphere is

$$s\Omega + MB \to 0 \quad \text{as} \quad r \uparrow r_o. \tag{2.11}$$

On the inner boundary, the complete solution of the Hartmann layer equations, which satisfy the boundary conditions (2.5a,b), is

$$B \approx B_i + \frac{1}{M|B_{ri}|}\left(\frac{\partial B}{\partial r}\right)_i \left\{1 - \exp\left[-M|B_{ri}|(r - r_i)\right]\right\}, \tag{2.12a}$$

$$\Omega \approx 1 + \frac{1}{sB_{ri}}\left(\frac{\partial B}{\partial r}\right)_i \left\{1 - \exp\left[-M|B_{ri}|(r - r_i)\right]\right\}, \tag{2.12b}$$

provided that

$$M|B_{ri}|\,|B_i| \gg \left|\left(\frac{\partial B}{\partial r}\right)_i\right|, \tag{2.12c}$$

where B_i and $(\partial B/\partial r)_i$ denote the values of B and its radial derivative inside (but at the boundary of) the solid conductor, while B_{ri} denotes the radial component of $\boldsymbol{B}_M$

https://doi.org/10.1017/S0022112001006711 Published online by Cambridge University Press

normal to the boundary at the location (s_i, z_i). This yields the mainstream boundary conditions

$$B \to B_i + \frac{1}{M|B_{ri}|}\left(\frac{\partial B}{\partial r}\right)_i, \quad \Omega \to 1 + \frac{1}{s_i B_{ri}}\left(\frac{\partial B}{\partial r}\right)_i \quad \text{as} \quad r \downarrow r_i, \tag{2.12d}$$

on the inner sphere.

The mainstream solution, that satisfies the symmetry conditions, $\Omega(s,-z) = \Omega(s,z)$, $B(s,-z) = -B(s,z)$ and the Hartmann jump conditions (2.11), (2.12), is

$$\mathscr{F}(A) = 1 \quad \text{everywhere} \quad (\text{except on} \quad A = A_Q = 1/2r_o) \tag{2.13a}$$

and

$$\mathscr{G}(A) = \begin{cases} A/A_Q & \text{in region } \mathscr{P}\text{: } 0 \leqslant A < A_Q \\ 0 & \text{in region } \mathscr{E}\text{: } A_Q < A \leqslant 1/2r_i \end{cases} \tag{2.13b}$$

(cf. Starchenko 1997, equation (79)). In applying (2.12*d*), we have assumed that $(1/B_i)\,(\partial B/\partial r)_i$ is of order unity, i.e. the radial length scale adopted by the potential solution inside the solid sphere is the same as the latitudinal length scale on its surface. So, since $B = O(M^{-1})$, the mainstream boundary condition (2.12*d*) reduces to $\Omega = 1 + O(M^{-1})$ as $r \downarrow r_i$. Consequently, the terms neglected in our application of the boundary conditions (2.11) and (2.12*d*) are both $O(M^{-1})$ consistent with our assumption (2.8). Note, however, that our error estimates are larger ($O(M^{-1/2})$) near Q, where the $\mathscr{C}$-line shear layer has a short $O(M^{-1/2})$ length scale, but the inequality (2.12*c*) is still met comfortably.

From (2.8*b*) and (2.13*b*) we deduce that the total electric current flowing outwards in the polar region $\mathscr{P}$ is

$$J_{\text{out}} := 2\pi(sB)_{A=A_Q} = -\pi/\mathscr{M} \tag{2.14}$$

(see (2.2)). Since none flows in the equatorial region $\mathscr{E}$, it is all returned along the $\mathscr{C}$-line shear layer.

We performed direct simulations of equations (2.3) up to Hartmann number $2\mathscr{M} := M/r_o^2 = 10^4$ for the radius ratio $r_i/r_o = 0.35$. In order to achieve better comparison with the asymptotics, we considered an initial value problem in which we reinstated inertia into (2.3*a*) by replacing the zero on its right-hand side by $\partial\Omega/\partial t$. It is important to appreciate that this is purely a device to aid convergence and only the final steady state is of interest. The two scalars Ω and B are represented as

$$\Omega = \sum_0^L \Omega_l(r) \mathrm{P}^1_{2l+1}(\cos\theta), \quad B = \sum_1^L B_l(r) \mathrm{P}^1_{2l}(\cos\theta), \tag{2.15a,b}$$

where θ is the colatitude. We calculated B_l and Ω_l on a radial grid stretched so that inner and outer Hartmann layers are well resolved. For $M/r_o^2 = 10^4$ we employed very high resolution (5000 points in radius and harmonics up to $L = 220$). The solutions in meridional planes are illustrated in figure 2. The constancy of sB on magnetic field lines in the polar region $\mathscr{P}$ implied by (2.13*b*) is clear. The absence of contours of constant sB in $\mathscr{E}$ and Ω in both $\mathscr{P}$ and $\mathscr{E}$ is consistent with (2.13). Evidently a free shear layer remains across the dividing field line $\mathscr{C}$: $A = A_Q$, where the mainstream approximations break down. Of course, as this layer thins with increasing M the global resolution of the spectral method becomes more and more difficult to implement and the boundary layer approach is then more attractive. For the boundary layer treatment of the shear layer, the Alfvén variables $V_\pm$ are more

https://doi.org/10.1017/S0022112001006711 Published online by Cambridge University Press

relevant than Ω and B, which is why contours of their constant values are portrayed also on figure 2. We discuss the nature of this free shear layer in the following section.

3. The shear layer $\mathscr{C}$

For reasons that will become clear when we study the equatorial Hartmann layer on the outer sphere in § 5, we introduce the notion of a $\mathscr{C}_M$-field line. It is defined to be the field line $\mathscr{C}_M$: $A = A_M := 1/2r_M$, where $r_M < r_o$ is chosen for our convenience later to be a function of M with the property that $r_M \uparrow r_o$ as $M \to \infty$. More specifically it is a field line that emerges from inside the equatorial Hartmann layer and so $r_o - r_M = O(M^{-2/3})$, which remains small compared to the shear layer thickness $O(M^{-1/2})$.

Points on the $\mathscr{C}_M$-line may be defined parametrically by

$$s = r_M \zeta^{3/2}, \quad z = r_M \zeta (1-\zeta)^{1/2}, \tag{3.1a}$$

where

$$\zeta = r/r_M, \quad \text{and} \quad \zeta_{Mi} = r_i/r_M. \tag{3.1b}$$

An important weighted measure of distance along the line is

$$\begin{aligned} \alpha(\zeta) &= -2\int_{E_M} s^2 \boldsymbol{B}_M \cdot \mathrm{d}\boldsymbol{x} = 2\int_{E_M} s^2 \,\mathrm{d}\Phi \\ &= -2\int_1^\zeta \frac{1-\frac{3}{4}\zeta}{(1-\zeta)^{1/2}}\,\mathrm{d}\zeta = (2-\zeta)\sqrt{1-\zeta}, \end{aligned} \tag{3.2}$$

where E_M: $(r_M, 0)$ is the intersection of the $\mathscr{C}_M$-line with the equatorial plane. Thus the weighted distance along $\mathscr{C}_M$ from E_M to its intersection Q_M: (s_{Mi}, z_{Mi}) with the inner sphere is $\alpha_{Mi} := \alpha(\zeta_{Mi})$. Thus we normalize this distance by introducing the coordinate l_M defined by

$$l_M := \int_{Q_M} s^2 \boldsymbol{B}_M \cdot \mathrm{d}\boldsymbol{x} \Big/ \int_{Q_M}^{E_M} s^2 \boldsymbol{B}_M \cdot \mathrm{d}\boldsymbol{x} = 1 - \frac{\alpha(\zeta)}{\alpha_{Mi}}, \tag{3.3a}$$

which has the property that it is zero at Q_M and unity at E_M. Distance normal to $\mathscr{C}_M$ is measured by the stretched flux function coordinate

$$n_M := \sqrt{2M/\alpha_{Mi}}(-A + A_M). \tag{3.3b}$$

Throughout the remainder of this section we consider only the limiting case $r_M = r_o$.

3.1. *The boundary layer formulation*

We adopt boundary layer coordinates $(l, n) \equiv (l_M, n_M)$ in the limit $M \to \infty$. They are

$$l := 1 - \alpha(\zeta)/\alpha_i, \quad n := \sqrt{2M/\alpha_i}(-A + A_Q), \tag{3.4a,b}$$

where

$$\alpha_i := 2\int_Q^{E_o} s^2 \boldsymbol{B}_M \cdot \mathrm{d}\boldsymbol{x} = \alpha(\zeta_i) \quad \text{with} \quad \zeta_i := r_i/r_o. \tag{3.4c}$$

In terms of ζ_i the inner and outer spherical boundaries are located at

$$r_i = \zeta_i/(1-\zeta_i) \quad \text{and} \quad r_o = 1/(1-\zeta_i). \tag{3.4d}$$

https://doi.org/10.1017/S0022112001006711 Published online by Cambridge University Press

Our choice of sign in the definition of n ensures that n is positive in $\mathscr{P}$ and negative in $\mathscr{E}$. Relative to the boundary layer coordinates (l, n), the boundary layer approximations of (2.10) yield

$$\frac{\partial V_\pm}{\partial l} \pm \frac{\partial^2 V_\pm}{\partial n^2} = \frac{1}{s}\frac{\partial s}{\partial l} V_\mp, \quad \text{where} \quad s(l) = r_o \zeta^{3/2} \tag{3.5a,b}$$

is defined implicitly as a function of l via (3.2) and (3.4a). The pair of parabolic partial differential equations (3.5a) are coupled by the term on the right-hand side, which arises due to curvature effects. The strength of the coupling is determined by the size of the coefficient

$$\frac{1}{s}\frac{\partial s}{\partial l} = \frac{3\alpha_i}{4}\frac{\sqrt{1-\zeta}}{\zeta\left(1-\frac{3}{4}\zeta\right)}. \tag{3.5c}$$

Solutions of (3.5a) are required that match with the mainstream solution (2.8). Expressed in our boundary layer coordinates, (2.13) determines the boundary conditions

$$V_\pm \to \begin{cases} s \mp (r_o^2/s)\left(1-\sqrt{\alpha_i/\mathscr{M}}\, n\right) & \text{as} \quad n \uparrow \infty \\ s & \text{as} \quad n \downarrow -\infty \end{cases} \tag{3.6}$$

on $0 < l < 1$, remembering that $s = s(l)$ and $\mathscr{M} = M/2r_o^2$.

To obtain the inner-sphere boundary conditions at $l = 0$, we need to consider the Hartmann layer at Q. Since the shear layer thickness is $O(M^{-1/2})$, that is the latitudinal length scale imposed on B at the surface of the solid inner conductor. The potential solution has the same radial scale and so we estimate that $(\partial B/\partial r)_i = O(M^{1/2}B_i) = O(M^{-1/2})$. Consequently, the Hartmann jump condition (2.12d) becomes $\Omega = 1 + O(M^{-1/2})$, which determines the condition

$$V_- + V_+ = 2s_Q + O(M^{-1/2}) \tag{3.7}$$

at $l = 0$ on the inner sphere.

The situation on the outer sphere is rather more delicate and we need to be aware of its location $\mathscr{S}_o$: $s = s_o(z)$ relative to our boundary layer coordinates. On $\mathscr{S}_o$, the value A_o of A satisfies $A_Q - A_o = z^2/2r_o^3$. Since the $\mathscr{C}$-line and $\mathscr{S}_o$ are tangent to each other at E_o, where $l = 1$, we may assume that, at given l close to unity, we may make the approximations $z \sim r_o(1-\zeta)^{1/2}$ and $\alpha \sim (1-\zeta)^{1/2}$. In this way we obtain, using (3.4a), the approximate results

$$A_o - A_Q \sim \tfrac{1}{2}(1-\zeta)/r_o \quad \text{and} \quad 1 - l \sim \sqrt{1-\zeta}\Big/\alpha_i, \tag{3.8a,b}$$

which together with (3.4b) determines the approximate location

$$n_o = \alpha_i^{3/2}\mathscr{M}^{1/2}(1-l)^2 \tag{3.8c}$$

of the outer-sphere boundary $\mathscr{S}_o$: $n = n_o(l)$. Evidently $\mathscr{S}_o$ eats into the boundary layer up to a distance $|1-l| = O(M^{-1/4})$, as illustrated on figure 7 below. Fortunately this distance tends to zero as $M \to \infty$ and so correct to lowest order the outer-sphere boundary conditions can be applied at $l = 1$.

In the neighbourhood of the equator E_o, the outer-sphere Hartmann jump condition (2.11) requires V_+, to vanish, while symmetry demands that B vanishes on $z = 0$.

https://doi.org/10.1017/S0022112001006711 Published online by Cambridge University Press

Together they yield the boundary conditions

$$V_+ = \begin{cases} 0 & \text{for} \quad n \geqslant 0 \\ V_- \equiv r_o \left(1 - \sqrt{\alpha_i/\mathscr{M}n}\right)^{-1} [1 + \Omega_S] & \text{for} \quad n < 0 \end{cases} \tag{3.9a,b}$$

at $l = 1$. Here we have introduced

$$\Omega_S(n) \equiv \Omega - 1, \tag{3.9c}$$

which measures super-rotation on the equatorial plane in the vicinity of E_o.

In addition to the $O(M^{-1/2})$ errors introduced by ignoring the Hartmann layer corrections at $l = 0$ and the higher-order matching terms as $|n| \to \infty$ on $0 < l < 1$, more substantial errors $O(M^{-1/3})$ are incurred at $l = 1$ through not considering the small equatorial Hartmann boundary layer ($|1 - l| = O(M^{-1/3})$ and $n = O(M^{-1/6})$), see figure 7 below. We rectify that deficiency in § 5.

We solved the boundary layer equations (3.5*a*) numerically subject to the lowest-order boundary conditions

$$V_\pm \to \begin{cases} s \mp (r_o^2/s) & \text{as} \quad n \uparrow \infty \\ s & \text{as} \quad n \downarrow -\infty \end{cases} \tag{3.10}$$

on $0 < l < 1$,

$$V_- + V_+ = 2s_Q \tag{3.11}$$

at $l = 0$, and

$$V_+ = \begin{cases} 0 & \text{for} \quad n \geqslant 0 \\ V_- \equiv r_o [1 + \Omega_S] & \text{for} \quad n < 0 \end{cases} \tag{3.12}$$

at $l = 1$ on the outer sphere, where the $O(M^{-1/2})$ terms appearing in (3.6), (3.7) and (3.9*a*) have been neglected. Results for the shell radius ratio $\zeta_i = 0.35$ employed for figure 2 are illustrated in figure 3. The curves of constant V_+ clearly indicate how it is advected from the singularity at the equator of the outer sphere E_o: $l = 1$ in the direction of decreasing l. It is essentially reflected at the inner sphere at Q: $l = 0$ and is returned as $2s_Q - V_-$ in the direction of increasing l. The advection–diffusion equations (3.5*a*) for $V_\pm$ are coupled by the source term $(1/s)(\partial s/\partial l)V_\mp$ on their right-hand side. This source term appears to be responsible for the 'nose-like' structures visible on the contours of constant $V_\pm$ for the large Hartmann number solutions in figure 2; they are clearly faithfully reproduced by the boundary layer solutions shown in figure 3.

The value $-B = r_o V_-/2M$ on the outer sphere for $l = 1$ is of some interest. It reduces from $-B = r_o/M$ as $n \uparrow \infty$ to $-B = r_o(1 + \Omega_S(0))/2M$ as $n \downarrow 0$. The fact that it is not zero determines the strength of the equatorial current source

$$J_{\text{source}} = -\tfrac{1}{2}\pi [1 + \Omega_S(0)]/\mathscr{M} = \tfrac{1}{2}[1 + \Omega_S(0)]J_{\text{out}}, \tag{3.13}$$

which emanates from the equatorial Hartman layer, where $n = O(M^{-1/6})$ (see § 6 below). The remaining current $J_{\text{out}}[1 - \Omega_S(0)]/2$ is returned directly into the shear layer ($n = O(1)$) from the Hartmann layer itself, where $n \gg M^{-1/6}$. This feature is clearly portrayed by the contours of $-MsB =$ constant in figure 3; some contours stem from the source, while others originate from the Hartmann layer at $l = 1$. There is also evidence of this partitioning of the return current into the source J_{source} and the

https://doi.org/10.1017/S0022112001006711 Published online by Cambridge University Press

continuous distribution $J_{\rm out} - J_{\rm source}$ from the full numerics for the case $M/r_o^2 = 10^4$ portrayed in figure 2.

3.2. *The narrow gap limit*

Though the boundary layer problem posed can only be solved numerically in general, some analytic progress can be made in the narrow gap limit

$$\varepsilon = (r_o - r_i)/r_o \ll 1, \tag{3.14a}$$

for which we may make the estimates

$$\frac{r_o - s}{r_o} = O(\varepsilon) \quad \text{and} \quad \frac{1}{s}\frac{\partial s}{\partial l} = O(\varepsilon) \quad \text{noting that} \quad 1 - \zeta_i = \varepsilon. \tag{3.14b}$$

Upon neglecting the $O(\varepsilon)$ terms in the boundary layer equations (3.5a), they then decouple and can be solved successively. Even though the ensuing system is relatively simple, it retains sufficient complexity to demonstrate the super-rotation phenomena. So our prime objective here is to determine the unknown super-rotation $\Omega_S(n)$.

We take (3.12) as our initial data $V_-(n,1) = r_o[1 + \Omega_S(n)]$ at E_o and solve the diffusion problem on $0 < 1 - l < 1$ for V_+. Its value $V_+(n,0)$ at Q provides, via (3.11), the initial data $V_-(n,0) = 2 - V_+(n,0)$ for V_+ on $0 < l < 1$. The solution to both problems can be expressed in the form

$$\frac{V_\pm}{r_o} = 1 \mp \tfrac{1}{2}\,\mathrm{erfc}\left(\frac{-n}{\sqrt{4(1 \mp l)}}\right) \pm \frac{1}{\sqrt{4(1 \mp l)\pi}} \int_{-\infty}^{0} \Omega_S(n') \exp\left(-\frac{(n-n')^2}{4(1 \mp l)}\right) \mathrm{d}n'. \tag{3.15}$$

The requirement, that the final value $V_-(1,n)$ for $n \leqslant 0$ at E_o is the same as the initial value of $V_+(1,n)$ there, leads to the integral equation

$$\Omega_S(n) = \tfrac{1}{2}\,\mathrm{erfc}\left(\frac{-n}{\sqrt{8}}\right) - \frac{1}{\sqrt{8\pi}} \int_{-\infty}^{0} \Omega_S(n') \exp\left(-\frac{(n-n')^2}{8}\right) \mathrm{d}n', \tag{3.16}$$

for $n \leqslant 0$, whose solution in turn determines the complete solution (3.15). In turn, the corresponding values of $s\Omega = (V_+ + V_-)/2$ and $B = (V_+ - V_-)/2M$ (see (2.9)) are readily obtained.

For $n < 0$, the solution of the diffusion problem can be expressed in terms of normal modes periodic in l of half period $l = 2$. Such separable solutions exist with

$$\Omega_S(n) = Re\left\{\sum_{k=0}^{\infty} \hat{\Omega}_k \exp\left[(1+\mathrm{i})\sqrt{(2k+1)\pi}\,\frac{n}{2}\right]\right\} \quad \text{on} \quad n < 0. \tag{3.17a}$$

Here the complex constants $\hat{\Omega}_k$ are the coefficients of the Fourier expansion of a periodic $\mathscr{C}$-line function, which reverses sign under the shift $l \to l + 2$ and is defined by $r_o^{-1}V_+(0, 1-l) - 1$ on $0 \leqslant l \leqslant 1$ and $1 - r_o^{-1}V_-(0, l-1)$ on $1 \leqslant l \leqslant 2$. Of course, the values of $\hat{\Omega}_k$ are unknown, but the form of (3.17a) does provide useful information about the large $-n$ behaviour, namely that

$$\Omega_S(n) \sim |\hat{\Omega}_0| \exp\left(\tfrac{1}{2}\sqrt{\pi}\,n\right) \cos\left(\tfrac{1}{2}\sqrt{\pi}\,n - \varphi_S\right) \quad \text{as} \quad n \downarrow -\infty, \tag{3.17b}$$

where $\hat{\Omega}_0 = |\hat{\Omega}_0| \exp(-\mathrm{i}\varphi_S)$. Essentially, Ω_S oscillates with period $4\sqrt{\pi}$ and decays exponentially in the $-n$-direction.

Though (3.17a) can be used as the basis of a method of solution, it is perhaps more instructive to solve (3.16) by successive iteration. This gives a series expansion

https://doi.org/10.1017/S0022112001006711 Published online by Cambridge University Press

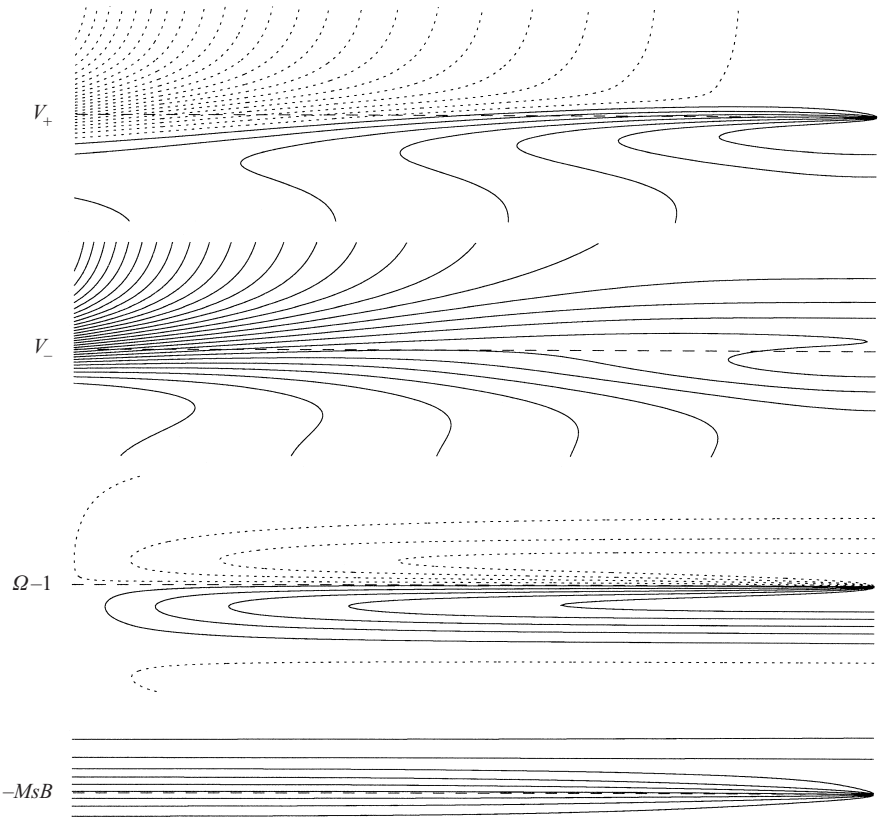


FIGURE 3. The numerical solution of the boundary layer equations (3.5*a*) in the l,n-plane for the radius ratio $r_i/r_o = 0.35$ of figure 2. The l-axis $0 \leqslant l \leqslant 1$ is identified by the horizontal dashed lines; the vertical extent is $-15 \leqslant n \leqslant 15$. As in figure 2, positive (negative) isovalues are indicated by the continuous (dotted) lines.

whose first two terms are

$$\Omega_S(n) = \frac{1}{2}\left[\operatorname{erfc}\left(\frac{-n}{\sqrt{8}}\right) - \frac{1}{\sqrt{8\pi}}\int_{-\infty}^{0} \operatorname{erfc}\left(\frac{-n'}{\sqrt{8}}\right)\exp\left(-\frac{(n-n')^2}{8}\right)\mathrm{d}n' + \cdots\right] \tag{3.18a}$$

which reduces to

$$\Omega_S(n) = \frac{3}{4}\operatorname{erfc}\left(\frac{-n}{\sqrt{8}}\right) - \operatorname{erfc}\left(\frac{-n}{4}\right)\left[\frac{1}{2} - \frac{1}{8}\operatorname{erfc}\left(\frac{-n}{4}\right)\right] + \cdots. \tag{3.18b}$$

The numerical solution for $V_+(1,n)/r_o = 1 + \Omega_S(n)$ obtained by taking the first two terms of (3.18) is illustrated by the dashed curve on figure 4, which according to (3.18*b*) terminates with $\Omega_S = 3/8$ at $n = 0$.

The iterated solution agrees with the numerical solution of the boundary layer equations and they are also shown on figure 4. As n is increased from $-\infty$, the value of Ω_S decreases slightly from zero to a minimum $\Omega_S \approx -0.0070$ at $n \approx -4.3636$ and then increases monotonically through zero at $n \approx -3.4376$. The separation (≈ 0.93) between the minimum and zero of Ω_S is in excellent agreement with the eighth period $\sqrt{\pi}/2 (\approx 0.89)$ predicted by the large $-n$ asymptotic result (3.17*b*). Then Ω_S continues to increase, terminating at $n = 0$ with the value $\Omega_S(0) \approx 0.4139$. This lies within the

https://doi.org/10.1017/S0022112001006711 Published online by Cambridge University Press

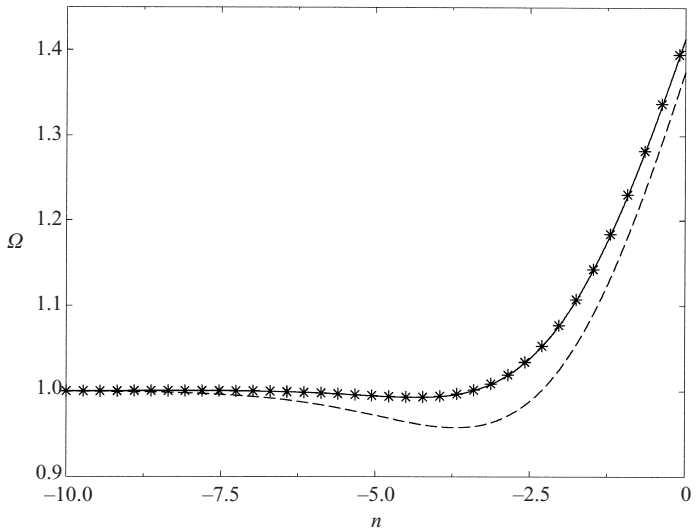


FIGURE 4. The angular velocity $1 + \Omega_S(n)$ on the equatorial plane plotted *vs.* n in the narrow gap limit $\varepsilon \ll 1$. The dashed line denotes the two-term solution (3.18), the continuous line denotes its iteration to 100 terms and the stars denote the numerical solution of system (4.1).

range $0.375 < \Omega_S(0) < 0.5$ suggested by the single-term and two-term expansions of (3.18*a*), which by the alternating nature of the series naturally bound the realized value. Of greater significance is the fact that $\Omega_S > 0$ in the range $-3.4376 < n \leqslant 0$. This feature is obvious even from the simple first term of the series expansion (3.18*a*), while the region of small negative Ω_S is suggested by the two-term representation (3.8*b*).

Our semi-analytic treatment of the narrow gap limit isolates the key mechanisms responsible for super-rotation. In particular, curvature effects, which we neglected in (3.14), are evidently unnecessary. Instead, we need to examine carefully how the electric current circuits are closed inside the electrically conducting fluid; we discuss this issue in the wide gap context in § 4.2 below.

In the next section we describe the numerical procedures adopted to solve the shear layer boundary layer problem. We discuss in more detail the nature of the results and make quantitative comparisons with the numerical solution of the complete governing equations (2.3) illustrated in figure 2 at finite M.

4. Numerical solution of the $\mathscr{C}$-boundary layer equations

The numerical solution of (3.5*a*) subject to the boundary conditions (3.10), (3.11) and (3.12) can be achieved by successively relaxing (3.5a_+) and (3.5a_-). We chose to use a finite difference scheme, well suited for this geometry. It consisted of a second-order scheme to compute the diffusion along n, and an up-wind first-order scheme to compute advection in l.

4.1. *Narrow gap limit*

The solution of the uncoupled system

$$\frac{\partial V_\pm}{\partial l} \pm \frac{\partial^2 V_\pm}{\partial n^2} = 0 \tag{4.1}$$

https://doi.org/10.1017/S0022112001006711 Published online by Cambridge University Press

appropriate to the narrow gap limit does not raise any particular difficulties. We only need to reduce the infinite domain in n to a finite computational domain. Solutions were obtained subject to two distinct sets of boundary conditions at the upper and lower n-boundaries. On the one hand, we applied Dirichlet boundary conditions and, on the other, Robin boundary conditions (exponential decrease). We checked that our computational domain was large enough for both approaches to give the same results. By this device numerical solutions were obtained (see the stars of figure 4) that are in excellent agreement with the iterated analytical solution (3.18) of § 3.2.

4.2. *Wide gap limit*

The numerical solution of the coupled system (3.5*a*) requires some additional care.

As $n \to \pm\infty$, our boundary conditions (3.10) require that n-derivatives vanish. There $V_\pm$ solves

$$\frac{\partial V_\pm}{\partial l} = \frac{1}{s}\frac{\partial s}{\partial l} V_\mp \tag{4.2}$$

with diffusion neglected and its solution is, of course, that defined by (3.10) as $n \to \pm\infty$. In the case of the discrete analogue of (4.2), the boundary condition (3.10) as $n \downarrow -\infty$ is a solution but the boundary condition (3.10) as $n \uparrow \infty$ is not; this is due to the nature of the up-wind discrete operator. Indeed, the error thus introduced if (3.10) is used as the numerical boundary condition does not let the successive relaxations reach a steady solution and the iterative resolution diverges. To overcome this difficulty, we replaced (3.10) as $n \to +\infty$ with the numerical solution of (4.2) imposing $V_+ = 0$ at $l = 1$ and $V_- = 2s_Q - V_+$, at $l = 0$. This numerical boundary condition is consistent in the sense that it tends to (3.10) as the number of l-points tends to infinity.

The numerical approximation of (3.5*a*) itself has inherent difficulties. We add artificial diffusion (often referred to as 'numerical diffusion') to this equation in the l-direction by use of the up-wind operator. This diffusion was kept small by using a large number of points (up to 8000) in this l-direction. For that, the difference between the numerical and exact boundary condition mentioned above is then less that 1%. We employed 600 points in the n-direction and results for the case $\zeta_i = 0.35$ are illustrated on figure 3; they should be compared to the full numerical solution of (2.3) illustrated in figure 2.

A more quantitative comparison between the boundary layer solution and the full numerics is possible by looking at the cross-sections of the shear layer at various values of l as illustrated in figure 5 for the case $\zeta_i = 0.35$. Our boundary layer equations have been solved subject to the conditions that all quantities tend to constants as $n \to \infty$ (see (3.10)). Nevertheless, it is quite clear that the numerical results at finite Hartmann number veer away from those constant values as $n \uparrow \infty$. This is consistent with the $O(M^{-1/2})$ corrections present in the true boundary conditions (3.6). The termination of the finite-M curves at certain positive values of n reflects the fact that the cross-section has either reached the symmetry axis ($l = 0.1$) or the outer sphere $l = 0.4$ and $l = 0.7$; in the extreme case ($l = 1.0$) the outer boundary is reached at $n = 0$ in all cases. The abrupt drops in values of V_- visible in some cases for $l = 0.4$ and 0.7 are manifestations of the Hartmann layer on the outer boundary.

It is important to remember that contours of constant sB are electric current lines (see above (2.8)). In the mainstream region they are almost parallel to the meridional field lines (see (2.8)) and so produce no Lorentz force. That negative electric current

https://doi.org/10.1017/S0022112001006711 Published online by Cambridge University Press

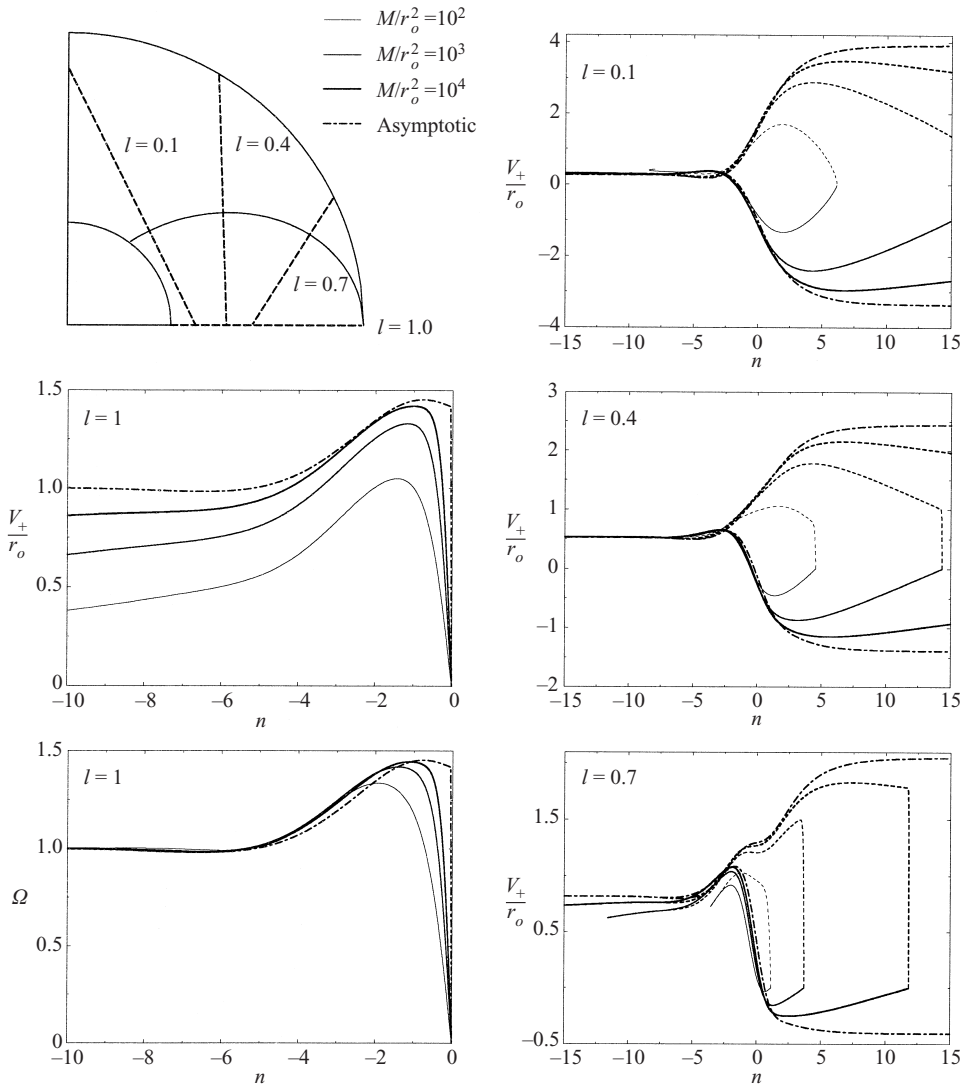


FIGURE 5. For caption see facing page.

($\boldsymbol{j}$ is directed inwards) is returned in the outer Hartmann boundary layer to the equator. Its total magnitude on entering the shear layer is $|J_{\text{out}}|$ (see (2.14)). A small fraction $|J_{\text{out}}|(1-\Omega_s(0))/2$ escapes directly into the shear layer but the larger fraction $|J_{\text{source}}| = |J_{\text{out}}|(1+\Omega_s(0))/2$ (see (3.3)) is returned from the small equatorial Hartmann layer, which on the scale of the shear layer is a point source. The consequences of that are clear in figure 3. The negative current J_{source} emerging from the source spreads with decreasing l ($\boldsymbol{j}$ is directed outwards). Whether the corresponding contours of constant sB cross the contours n =constant from below or above determines the sign of the Lorentz force $\boldsymbol{j}\times\boldsymbol{B}_M$. In figure 3 the contours of $-MsB$ have the correct inclination for negative n to accelerate the fluid. Another measure of the domain, in which the fluid is accelerated, is provided by figure 5. There acceleration occurs when $\partial^2\Omega/\partial n^2 < 0$, which is identifiable for moderate negative values of n. The cross-section $l = 1$ is particularly revealing in this respect, exhibiting features similar to those already seen

https://doi.org/10.1017/S0022112001006711 Published online by Cambridge University Press

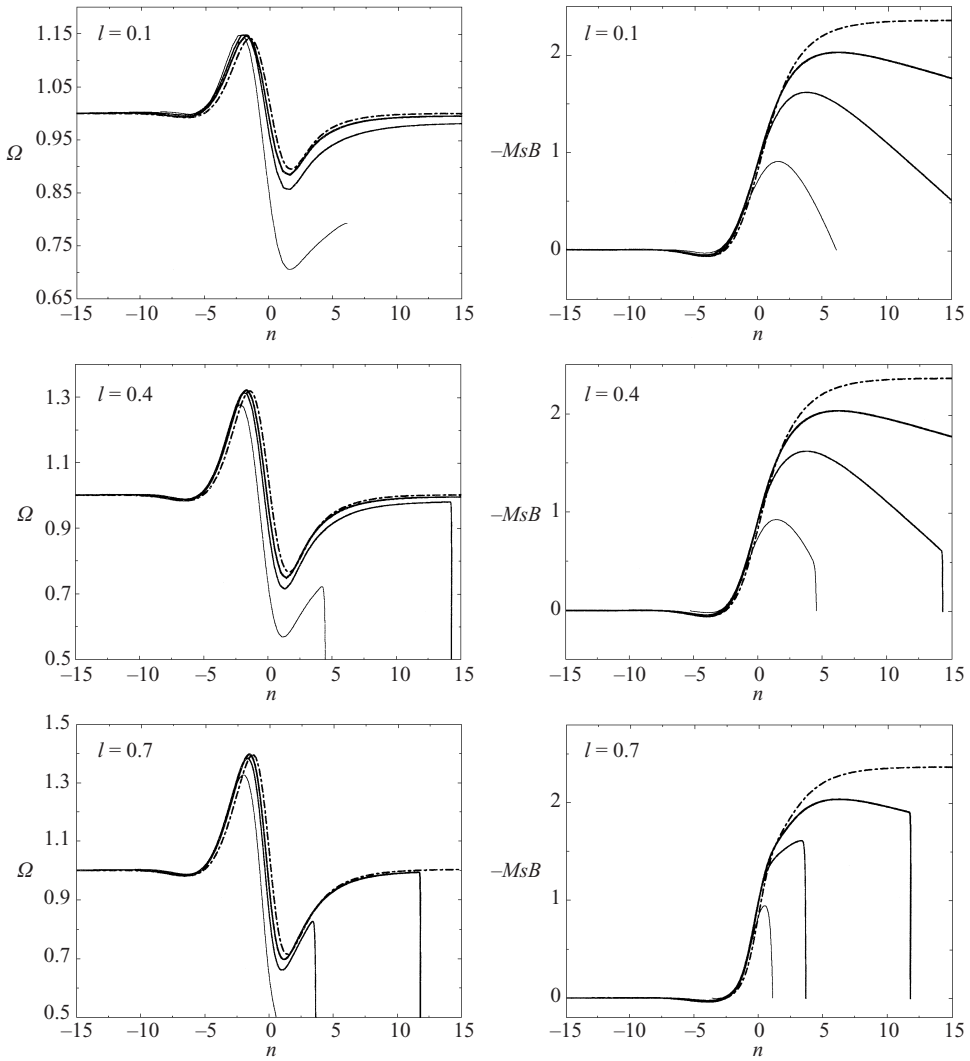


FIGURE 5. The quantities V_+/r_o, V_-/r_o, Ω and $-MsB$ plotted *vs.* n at $l = 0.1$, 0.4, 0.7 and 1.0 for the radius ratio $r_i/r_o = 0.35$. Numerical solutions of the governing equations (2.3) are shown for $M/r_o^2 = 10^2$, 10^3, 10^4 by continuous (except for V_-/r_o dashed) lines of increasing solidity; the numerical solutions of the boundary equations (3.5*a*) are identified by the short-long-dashed curves. The larger the value of M the closer the curve is to the asymptote.

in the narrow gap limit, and is well represented by the asymptotic solution. For that the value of Ω_S decreases slightly from zero at $n = -\infty$, as n is increased; it attains its minimum $\Omega_S \approx -0.01780$ at $n \approx -6.4776$, then increases monotonically through zero at $n \approx -5.1619$ to its maximum $\Omega \approx 0.4530$ at $n \approx -0.7663$, then finally decreasing and terminating at $n = 0$ with the value $\Omega_S(0) \approx 0.4147$ close to the value found in the narrow gap limit.

The fact that the maximum angular velocity Ω is found on the equatorial plane ($l = 1$) not at E_o ($n = 0$) but at a finite distance inside the fluid at $n \approx -0.7663$, is a curious feature special to the finite gap. It is therefore dependent on the coupling term $(1/s)(\partial s/\partial l)V_{\mp}$ on the right-hand side of (3.5*a*). The plots at $l = 0.7$ on figure 5

https://doi.org/10.1017/S0022112001006711 Published online by Cambridge University Press

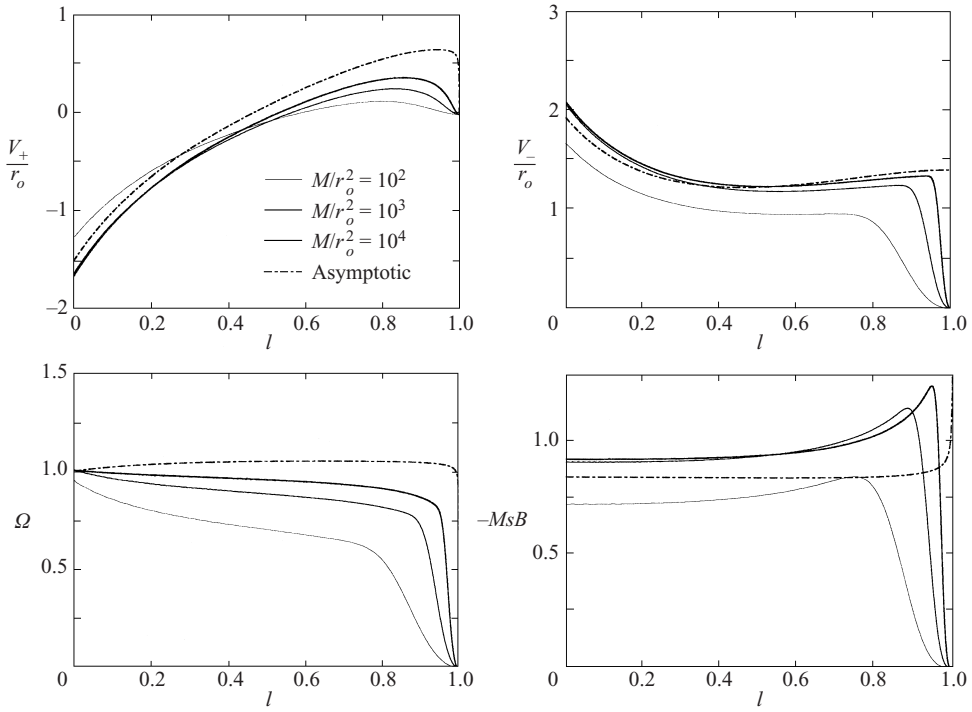


FIGURE 6. As for figure 5 (except for V_- now continuous) but plotted *vs.* l on the $\mathscr{C}$-line $n = 0$.

suggest that the value of V_+ being advected inwards from the equator acts as a sufficiently strong source to alter the outwardly advected V_- giving it a flattened profile at its centre. This is ultimately manifested by the interior local maximum on the equator. Another manifestation of the same effect is identified by an 'S'-shaped contour of V_- at the centre of the layer close to the equator $l = 1$ in figure 3.

An alternative and somewhat more testing comparison is made on figure 6, where quantities are plotted on the $\mathscr{C}$-line ($n = 0$). There some apparently substantial differences between the numerics and asymptotics are visible. The most obvious failure occurs in the neighbourhood of $l = 1$ and can be accounted for by noting that when $|1 - l| = O(M^{-1/3})$ the $\mathscr{C}$-line is inside the equatorial Hartmann boundary layer, where the shear layer boundary layer problem that we have solved ceases to be valid. Outside this equatorial layer it appears that our numerics converge slowly for large M.

Returning to figure 5, we notice that the Ω-profiles appear to be shifted by an amount consistent with a boundary layer displacement induced by the equatorial Hartmann layer. We explore this idea in the next section and isolate such a boundary layer displacement through solving the equatorial Hartmann layer problem. We then redraw the figure 5(a) for Ω at $l = 1$ in figure 9 below but with each finite-M curve displaced by its appropriate amount. In the same spirit, we draw figure 10 below equivalent to figure 6 but the results for the full numerical solution at each given M are plotted on the properly chosen displaced $\mathscr{C}_M$-line. The improvements obtained strongly support our contention that the leading-order corrections stem from a boundary layer displacement.

https://doi.org/10.1017/S0022112001006711 Published online by Cambridge University Press

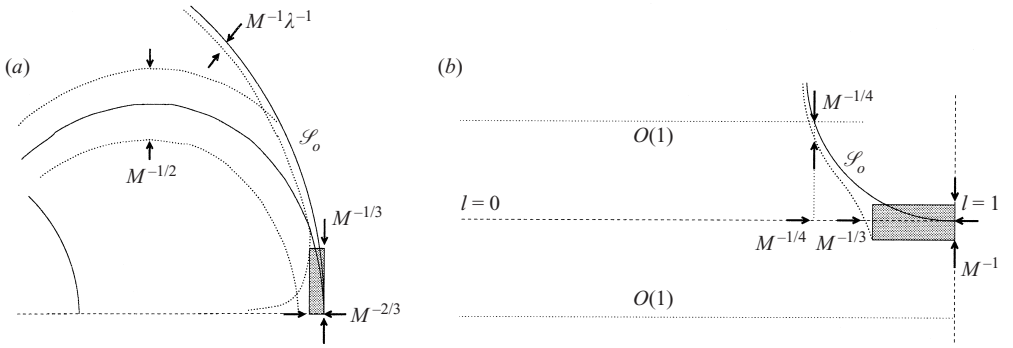


FIGURE 7. A schematic representation of the equatorial Hartmann layers and its neighbouring boundary layers on the outer-sphere boundary $\mathscr{S}_o$. Its relation to the $M^{-1/2}$ $\mathscr{C}$-shear layer and the outer sphere M^{-1} Hartmann layer are shown (*a*) in the meridional plane and (*b*) relative to the l, n boundary layer coordinates of the shear layer.

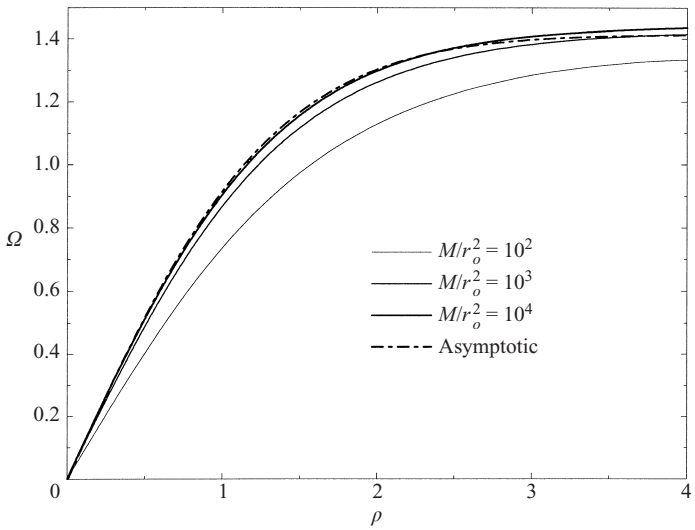


FIGURE 8. The angular velocity profiles Ω plotted *vs.* ρ in the equatorial Hartmann layer on the equator $\tau = 0$ for the radius ratio $r_i/r_o = 0.35$. The curves for $M/r_o^2 = 10^2, 10^3, 10^4$ are identified by continuous lines of increasing solidity, which for small ρ approach the asymptotic solution (5.12) given by the short-long dashed curves.

5. Equatorial Hartmann layer

The length scales for the equatorial Hartmann layer are dictated by the outer-sphere boundary shape (3.8) in the immediate vicinity of E_o and the form of the shear layer equations (3.5*c*). Together they suggest the change of variables

$$1 - l = \alpha_i^{-1} \mathscr{M}^{-1/3} \tau, \quad n = -\alpha_i^{-1/2} \mathscr{M}^{-1/6} \rho, \tag{5.1a,b}$$

for which the boundary $\mathscr{S}_o$: $n = n_o(l)$ (see (3.8*c*)) is transformed to

$$\xi := \rho + \tau^2 = 0. \tag{5.2}$$

The length scales of the equatorial boundary layer are therefore $|1 - l| = O(M^{-1/3})$ and $n = O(M^{-1/6})$ (or equivalently $r_o - s = O(M^{-2/3})$), as indicated on figure 7. With

https://doi.org/10.1017/S0022112001006711 Published online by Cambridge University Press

these estimates the coefficient $(1/s)(\partial s/\partial l)$ (3.5c) on the right-hand side of (3.5a) is $O(M^{-1/3})$. Therefore, the term on the right-hand side of (3.5a) is smaller than the large derivatives on the left-hand side by a factor $O(M^{-2/3})$ and may clearly be neglected, leaving

$$\frac{\partial V_\pm}{\partial \tau} \mp \frac{\partial^2 V_\pm}{\partial \rho^2} = 0. \tag{5.3}$$

The simplest way to formulate our boundary layer problem is to solve on the infinite interval $-\infty < \tau < \infty$ which includes the other half of the boundary layer in the southern hemisphere $z < 0$. In this way our symmetries imply that $V_\pm$ can be defined in terms of a single function $\Theta(\rho, \tau)$, which solves the diffusion equation

$$\frac{\partial \Theta}{\partial \tau} = \frac{\partial^2 \Theta}{\partial \rho^2} \quad \text{on} \quad \rho > -\tau^2 \tag{5.4}$$

as follows:

$$V_\pm(\rho, \tau) = r_o[1 + \Omega_S(0)]\,[1 - \Theta(\rho, \pm\tau)]. \tag{5.5}$$

The idea is simply that the value of V_- being advected in the shear layer down towards the equatorial Hartmann layer is given by $r_o[1 - \Omega_S(0)]$ as $\tau \uparrow \infty$, namely the leading-order approximation of it for $n = O(M^{-1/6})$. This provides our initial value unity for Θ as $\tau \downarrow -\infty$. It also provides our boundary condition as $\rho \uparrow \infty$. Since both B and Ω vanish on the boundary, our diffusion equation (5.4) must be solved subject to the boundary conditions

$$\Theta \begin{cases} = 1 & \text{on the outer sphere } \rho = -\tau^2 \\ \to 0 & \text{as} \quad \rho \uparrow \infty, \end{cases} \tag{5.6}$$

and the initial condition

$$\Theta = 0 \quad \text{for} \quad \rho > -\tau^2 \quad \text{as} \quad \tau \downarrow -\infty. \tag{5.7}$$

In order to make analytic progress, it is helpful use ξ (see (5.2)) and τ as our dependent variables rather than ρ and τ. Then in place of (5.4), Θ satisfies

$$\frac{\partial \Theta}{\partial \tau} + 2\tau \frac{\partial \Theta}{\partial \xi} = \frac{\partial^2 \Theta}{\partial \xi^2} \quad \text{on} \quad \xi > 0. \tag{5.8}$$

We see at once that the large negative-τ solution has the asymptotic form

$$\Theta = \exp(2\tau\xi) \quad \text{as} \quad \tau \downarrow -\infty. \tag{5.9}$$

Here the exponential simply defines a very thin boundary layer, which for our MHD problem corresponds to the Hartmann layer associated with V_- as it approaches the equator in the shear layer from above. As τ increases, the boundary layer width, $O(-1/\tau)$, thickens. Relative to the latitude $\lambda = \sin^{-1}(z/r_o)$, this corresponds to the radial width of the Hartmann layer thickening proportional to $O(|\lambda M|^{-1})$. The thickening stops at width $O(M^{-2/3})$, when $\lambda = O(M^{-1/3})$, which defines the dimensions of the equatorial Hartmann layer as illustrated in figure 7.

The layer detaches from the boundary at $\tau = 0$ and for large positive τ becomes the shear layer in the neighbourhood of the $\mathscr{C}$-line $\rho = 0$ or equivalently $\xi = \tau^2$. There it has the asymptotic form

$$\Theta = \frac{1}{2}\,\mathrm{erfc}\left(\frac{\rho - \delta}{\sqrt{4\tau}}\right) \quad \text{as} \quad \tau \uparrow \infty \tag{5.10}$$

https://doi.org/10.1017/S0022112001006711 Published online by Cambridge University Press

on $-\tau^2 < \rho < \infty$, where the constant δ of order unity is determined by the solution. To understand the nature of (5.10), we note that with $\delta = 0$ it is the solution of the diffusion equation (5.4) on the infinite interval $-\infty < \rho < \infty$ subject to the initial conditions $\Theta = 0$ on $\rho > 0$ and $\Theta = 1$ on $\rho \leqslant 0$ at $\tau = 0$. This is exactly the boundary condition which we employed at $l = 1$ in the previous § 4, to solve for the free shear layer. The point that we wish to stress is that, when we match the shear layer solution to the equatorial Hartmann layer solution, the shear layer is effectively triggered on the equator at $\rho = \delta$ rather than at $\rho = 0$. In other words, the effective $\mathscr{C}$-line is the $\mathscr{C}_M$-line, which intersects the equatorial plane at

$$n = -\alpha_i^{-1/2} \mathscr{M}^{-1/6} \delta \; ; \tag{5.11a}$$

it determines

$$(r_o - r_M)/r_M = \mathscr{M}^{-2/3} \delta \tag{5.11b}$$

entirely in terms of the local Hartmann number (2.2) appropriate to the equatorial Hartmann layer. We relegate the details of the calculation to the Appendix but note that complete solution (A1) and (A2) yields the result (A12), (A13). From them we deduce

$$\delta = 2 \int_0^\infty \frac{[\mathrm{Ai}(\sigma)]^2 + \sqrt{3}\mathrm{Ai}(\sigma)\mathrm{Bi}(\sigma)}{[\mathrm{Ai}(\sigma)]^2 + [\mathrm{Bi}(\sigma)]^2} \, \mathrm{d}\sigma \approx 1.2551, \tag{5.11c}$$

where Ai and Bi are the usual Airy functions.

The solution (A1), (A2) may also be used to determine the angular velocity

$$\Omega(\rho) = [1 + \Omega_S(0)] \, [1 - \Theta(\rho, 0)] \tag{5.12a}$$

on the equatorial plane, where

$$\Theta(\rho, 0) = \int_0^\infty \left\{ \mathrm{Ai}(\sigma) \left[\frac{\mathrm{Ai}(\rho + \omega^{-1}\sigma)}{\mathrm{Ai}(\omega^{-1}\sigma)} + \frac{\mathrm{Ai}(\rho + \omega\sigma)}{\mathrm{Ai}(\omega\sigma)} \right] + \mathrm{Ai}(\rho + \sigma) \right\} \mathrm{d}\sigma \tag{5.12b}$$

in which $\omega = \exp(\mathrm{i}2\pi/3)$. We plot Ω on figure 8 using the value

$$\Omega_S(0) = 0.4147\ldots \quad \text{for the case} \quad \zeta_i = 0.35 \tag{5.13}$$

determined by the free shear boundary layer calculation reported in § 4. The corresponding values of the angular velocity computed from the full numerical integrations at finite M are also portrayed for comparison.

In order to make a more faithful comparison with the shear layer boundary layer solution and the numerics, we take into account the displacement thickness determined by (5.11) in portraying the finite-M results in figures 9 and 10 below. By that we mean that each finite-M numerical solution is determined as a function of the shear layer boundary layer coordinates (l_M, n_M) defined by (3.3) which are based on the $\mathscr{C}_M$-line defined by $A_M = 1/2r_M$, where r_M given by (5.11b). At any given point in the shear layer, we note that $l - l_M$ is small, $O(M^{-2/3})$, so that the distinction between l_M and l is unimportant, while correct to lowest order we have

$$\begin{aligned} n - n_M &= -\left(\frac{r_o}{2}\right)^{1/3} \left(\frac{2}{\alpha_i}\right)^{1/2} M^{-1/6} \delta \\ &\approx -1.4101 M^{-1/6} \quad \text{for the case} \quad \zeta_i = 0.35, \end{aligned} \tag{5.14}$$

which though small is relatively large and significant.

In figure 9, we redraw the equatorial plot of Ω against n at $l = 1$ displayed in figure 5(a). Now each finite-M solution is plotted against n_M at $l_M = 1$, whereas the

https://doi.org/10.1017/S0022112001006711 Published online by Cambridge University Press

M/r_o^2	100	1000	10000	Asymptotic
$n_{\max}$	−1.95	−1.40	−1.12	−0.77
$\rho_{\max}$	3.74	3.94	4.63	
$\rho_{S\max}$	1.48	2.17	3.18	

TABLE 1. The location of the finite-M maxima of Ω in terms of the boundary layer coordinates $n_{\max}$, $\rho_{\max}$. The asymptotic boundary layer value $n_{\max} = -0.77$ is cast in terms of the equatorial Hartmann layer coordinate $\rho_{S\max}$.

asymptotic solution is left untouched. This plot is most revealing as it confirms that corrections arising from the displacement thickness give excellent agreement between the shear layer solution and the full numerics outside the thin equatorial Hartmann layer. Though good comparisons of Ω inside the equatorial Hartmann layer are also evident in figure 8, the lack of a clear asymptotic trend for large ρ can be attributed to the fact that we are not yet in a true asymptotic regime. This is highlighted by noting the locations $n = n_{\max}$ at which Ω (full numerics) and $1 + \Omega_S$ (the shear layer) are maximum on the equatorial plane and translating them into the boundary layer coordinate values $\rho = \rho_{\max}$ and $\rho_{S\max}$ respectively. We list these values in table 1. Thus the location where the curvature of the free shear layer solution is important remains within the equatorial Hartmann layer even for the largest value of M considered. The implication is that quadratic, as well as linear effects, are influencing the large-ρ trends visible in figure 8.

On figure 10, we repeat the plots of figure 6 but with one crucial difference: each of the finite-M numerical solutions is plotted versus l_M on its $\mathscr{C}_M$-line $n_M = 0$. Though necessary differences between the shear layer solution and the full numerics remain in the equatorial Hartmann layer near $l_M = 1$, the comparisons outside are far better than those reported in figure 6. Yet again the results confirm the reliability of the notion of a displacement thickness that we have developed.

Some bumps on the Ω-profiles can be identified near $l_M = 1$ on figure 10, where the $\mathscr{C}_M$-line $n_M = 0$ enters the equatorial Hartmann layer. These bumps were absent on the $\mathscr{C}$-lines $n = 0$ portrayed in figure 6. Thus these contrasting features provide information about the nature of the equatorial Hartmann layer at finite M.

6. Discussion

We have successfully resolved the mainstream and boundary layer structures, obtaining their solutions by a combination of analytical and numerical techniques. The cornerstone of our development has been the successful implementation of numerical methods to solve the unusual coupled advection–diffusion equations that govern the shear layer. The solution of that problem clearly accounts in a semi-analytic way (certainly in the narrow gap limit) for the phenomenon of super-rotation. The numerical solution of the complete governing equations at large M is also difficult. That results were obtained at sufficiently large M to obtain convincing agreement with the asymptotic theory was most reassuring.

From a more general point of view, the mechanism for super-rotation described in §4.2 hinges on the electric current flow in our system. Essentially, negative electric current flows outwards along field lines in the polar region $\mathscr{P}$ (total J_{out} see (2.14)), it

https://doi.org/10.1017/S0022112001006711 Published online by Cambridge University Press

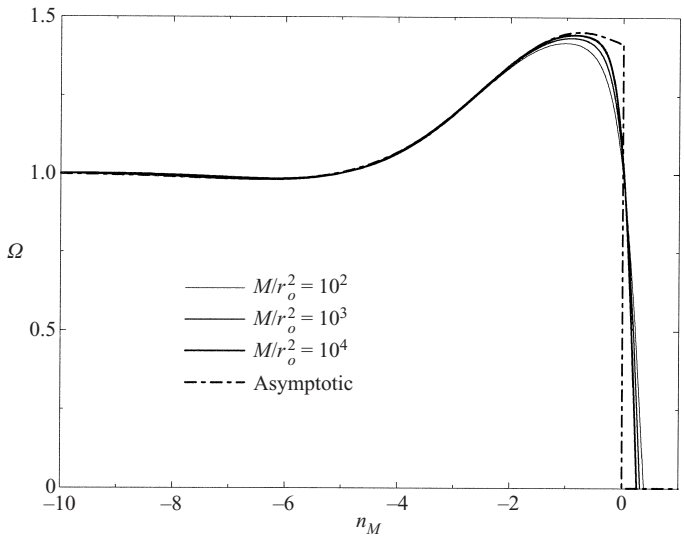


FIGURE 9. As in figure 5(*a*), except that Ω at each M is plotted *vs.* n_M at $l_M = 1$. Note that $n_M \equiv n$ for the asymptotic shear layer solution.

is carried down to the equator in the outer-sphere Hartmann layer and returns to the inner sphere along the $\mathscr{C}$-line shear layer. A substantial fraction J_{source} (see (3.13)), however, reaches the equatorial Hartmann layer, which effectively acts as a current source and thus as the essential mechanism leading to super-rotation. In particular, the current emitted from the source largely follows the $\mathscr{C}$-line but spreads laterally through diffusion. This leads to a Lorentz force, which is largely accelerating on the equatorial side and de-accelerating on the polar side. This phenomenon is well known in the context of channel flow, where current injected from electrodes, which are embedded in the channel boundary, attempts to follow the magnetic field lines (see Müller & Bühler 2001, figures 7.1 and 7.2).

Starchenko (1997) notes that the Hartmann jump condition (2.2*d*) can imply super-rotation in the fluid adjacent to the inner sphere, when $(1/s_i B_{ri})(\partial B/\partial r)_i > 0$ (see his equation (81)). That this is likely to happen in the equatorial region $\mathscr{E}$ is clear from the contours of constant sB inside the solid conducting sphere near the equator seen in our figure 1. Since Ω is constant on meridional field lines, small super-rotation, $O(M^{-1})$, should be present throughout $\mathscr{E}$. The Hartmann jump is stronger, $O(M^{-1/2})$, near Q at the end of the $\mathscr{C}$-line shear layer. Nevertheless, our analysis of the shear layer shows that current diffusion in the shear layer has the dominating $O(1)$ effect and that the Hartmann jump can be ignored. Thus Starchenko's argument is not able to account for the $O(1)$ super-rotation that we find and explain.

Hollerbach (2000) also considers numerically the cases in which the inner and outer spheres are either both insulating or both conducting. The key to understanding the dynamics of these configurations is the role played by the Hartmann layers. We limit our discussion to the later more dramatic conducting case for which the inner-sphere Hartmann layer has solution (2.12), while a similar solution pertains to the outer boundary. Now for our inner conducting and outer insulating problem, we can accept a small $O(M^{-1})$ azimuthal magnetic field B by virtually locking the angular velocity Ω of the mainstream flow to the rotation $\Omega = 1$ of the inner conducting sphere. When both the inner and outer solid spheres are conducting, that is no longer possible. Now

https://doi.org/10.1017/S0022112001006711 Published online by Cambridge University Press

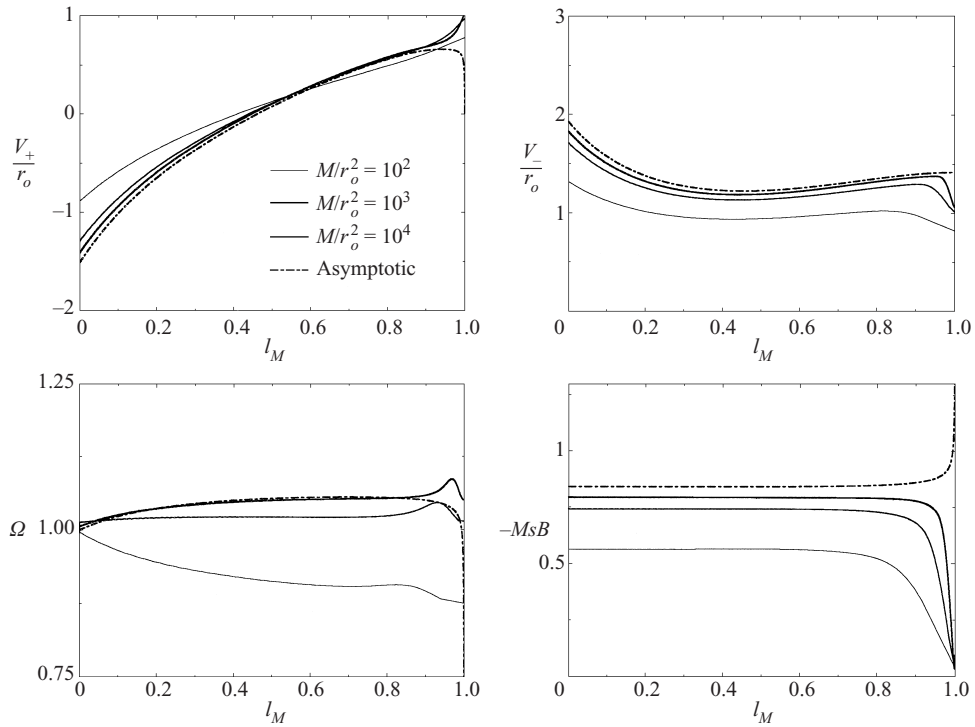


FIGURE 10. As in figure 6 (note that the Ω scale has been stretched), except that solutions at each M are plotted *vs.* l_M on each $\mathscr{C}_M$-line $n_M = 0$. Note that $l_M \equiv l$ for the asymptotic shear layer solution.

both Hartmann layers have to accept an $O(1)$ jump in the angular velocity, which is only achieved with a corresponding azimuthal magnetic field $B = O(1)$ (see (2.12*d*)). A correct physical explanation for this increase in magnitude of B was provided by Hollerbach (2000) in interpreting his numerical results for different boundary conditions. His explanation relies on two facts. First, for insulating outer boundaries, the electric current J_{out} flowing outwards along meridional magnetic field lines in the mainstream polar region $\mathscr{P}$ is transmitted to the equator inside the outer-sphere Hartmann layer, as we repeatedly stress. This leads to Lorentz forces that can achieve $O(1)$ angular velocity jumps for relatively small azimuthal magnetic fields. Secondly, for conducting outer boundaries, the electric currents leak out of the Hartmann layers into the solid conductor. So to obtain a sufficiently strong Lorentz force in the Hartmann layer capable of supporting the angular velocity jump, the entire current flow in the system must be increased by a large factor, $O(M)$.

We tentatively propose the following scenario for Hollerbach's conducting inner and outer spheres. In the mainstream, sB continues to be constant on meridional magnetic field lines, being zero in the equatorial region $\mathscr{E}$ and order unity ($O(1)$) in the polar region $\mathscr{P}$ (i.e. $O(M)$ larger than for our case (2.8*b*)). Then by the magnetic induction equation (2.3*b*), the resulting Ω is also $O(1)$ in the mainstream outside the shear layer $\mathscr{C}$ but no longer constant on field lines in the polar region $\mathscr{P}$. Furthermore, we propose that, unlike our problem, the bulk of the relatively large $O(1)$ electric current flow is returned in the mainstream polar region $\mathscr{P}$. This is accompanied by sB decreasing to zero as the $\mathscr{C}$-line is approached from the polar side. Provided that the decrease is linear, we estimate that the magnetic field, inside the shear layer

https://doi.org/10.1017/S0022112001006711 Published online by Cambridge University Press

on its $O(M^{-1/2})$ width, is $O(M^{-1/2})$. This means that his Alfvén variables would be $O(M^{1/2})$ larger than ours leading to a stronger super-rotation of magnitude $O(M^{1/2})$. This magnitude compares favourably with Hollerbach's (2000) numerical estimate of $O(M^{0.6})$. However, the general picture for the super-rotation mechanism in the shear layer, that we have proposed, should still apply, though, interestingly, this is despite the fact that only a relatively small fraction, $O(M^{-1/2})$, of the entire $O(1)$ current flow follows the $\mathscr{C}$-line. We stress that all these estimates stem from a preliminary theory, which forms the basis for a complete analysis of the problem at present in progress.

Considering that Roberts (1967*b*) had obtained, such a long time ago, an analytic solution for the case of an equatorial Hartmann layer with magnetic field lines bending towards the walls on leaving the equatorial plane, it is surprising that the alternative problem with the field lines bending away does not appear to have been addressed. Though the method of solution in the two cases is essentially the same, the specific details and answer are different. Significantly our derivation of the displacement width δ^* for the free shear layer enabled us to make considerable improvements with our quantitative comparisons with the full numerics. This leads us to believe that we have resolved correctly all the major boundary layer processes.

It should be stressed that a key feature which enables progress to be made with the equatorial boundary layer solution in § 5 is the insulating boundary condition that requires $B = 0$. By implementation of the zero boundary condition on both V_+ and V_-, the two diffusion equations (5.3) remain uncoupled. For more general boundary conditions that is not the case. Whatever the boundary conditions, the corresponding equatorial boundary layer solution only leads to low-order corrections; the dominant leading-order results are not dependent on this layer.

E. D. visited the School of Mathematical Sciences at the University of Exeter in September 1999, while A. M. S. visited IPGP in November 2000; both E. D. and A. M. S. wish to thank their respective host institutions for their hospitality and support. A. M. S. acknowledges support of PPARC grant GR/L40922 and INTAS grant 99-00348, through which he has benefited from discussions with Dr S. Starchenko. E.D. would like to thank Professor Y. Brenier and Dr D. Pissarenko for stimulating discussions about the shear layer problem (3.5), (3.10)–(3.12), while we are all grateful to Dr R. Hollerbach for useful discussions. Numerical resolution of this system was achieved on a Cray SV1 computer at the C.C.R.-Jussieu, whereas solutions of the complete governing equations where computed at the Service Commun de Calcul Intensif de l'Observatoire de Grenoble.

Appendix. The equatorial Hartmann layer solution

We adapt Roberts' (1967*b*) solution to a related problem of Hartmann flow down a circular pipe with a uniform transverse magnetic field applied (see also Waechter 1969). The common feature is the existence of points on the boundary at which the magnetic field is tangent. The problems differ in that our field lines bend away from the boundary into the fluid as the equator is left, whereas his effectively approach the boundary. Put another way, his problem would have been equivalent to ours if his fluid were outside rather than inside the pipe! So though the techniques involved in our solution are similar to his, the details are quite different.

Roberts' (1967*b*) solution relies on the preliminary change of variables

$$\Theta(\xi,\tau) = \exp(\tau\xi - \tfrac{1}{3}\tau^3)\,\Phi(\xi,\tau), \tag{A 1a}$$

https://doi.org/10.1017/S0022112001006711 Published online by Cambridge University Press

which satisfies (5.8) when

$$\frac{\partial^2 \Phi}{\partial \xi^2} - \xi \Phi = \frac{\partial \Phi}{\partial \tau}. \tag{A 1b}$$

Guided by Roberts' (1967*b*) analysis, we demonstrate that the solution of the problem specified by (5.4), (5.6) and (5.7) is

$$\Phi = \Phi_{-1} + \Phi_0 + \Phi_1, \tag{A 2a}$$

where

$$\Phi_n = \int_0^\infty \frac{\mathrm{Ai}(\sigma)\mathrm{Ai}(\xi + \omega^n \sigma)}{\mathrm{Ai}(\omega^n \sigma)} \exp(\omega^n \tau \sigma)\, \mathrm{d}\sigma \quad (\omega = \exp(\mathrm{i}2\pi/3)); \tag{A 2b}$$

here ω^{-1}, 1 and ω are the cube roots of unity. Note also that $\Phi_{-1} = \Phi_1^*$ for real ξ and τ, where the star denotes the complex conjugate. It is a trivial matter to verify that (A 2) satisfies (A 1*b*) by direct substitution. It only remains to show that the boundary conditions (5.6) and initial conditions (5.7) (also (5.9)) are met.

A key step in establishing the result (A 2) is to note that the boundary condition (5.6) $\Theta = 1$ at $\xi = 0$ is met simply because of the identity

$$\int_0^\infty \mathrm{Ai}(\sigma) \left[\exp\left(\omega^{-1}\tau\sigma\right) + \exp(\tau\sigma) + \exp(\omega\tau\sigma)\right] \mathrm{d}\sigma = \exp\left(\tfrac{1}{3}\tau^3\right). \tag{A 3a}$$

This is readily established using the power series representations of the exponentials and the identity

$$3\int_0^\infty \sigma^{3m} \mathrm{Ai}(\sigma)\, \mathrm{d}\sigma = \frac{(3m)!}{3^m m!} \quad \text{for} \quad m = 0, 1, 2, 3, \ldots\ . \tag{A 3b}$$

Here the case $m = 0$ is given by Abramowitz & Stegun (1964, equation (10.4.47)), while the cases $m \geqslant 1$ follow by mathematical induction using the property $\sigma \mathrm{Ai}(\sigma) = \mathrm{d}^2\mathrm{Ai}(\sigma)/\mathrm{d}\sigma^2$ and integrating by parts; Roberts (1967*b*) obtained a comparable result (his equation (49)) using integral properties of Bessel functions.

Since all the Airy functions in (A 2*b*) decay exponentially for large positive σ, it is self-evident that the solution (A 2*a*) satisfies the boundary condition $\Phi \to 0$ as $\xi \uparrow \infty$.

As a preliminary step to establish the initial condition (5.7) we note the alternative form

$$\Phi = \tilde{\Phi}_{-1} + \tilde{\Phi}_0 + \tilde{\Phi}_1, \tag{A 4a}$$

where

$$\tilde{\Phi}_n = \int_{\omega^{-n} v_s}^\infty \frac{\mathrm{Ai}(\sigma)\mathrm{Ai}(\xi + \omega^n \sigma)}{\mathrm{Ai}(\omega^n \sigma)} \exp(\omega^n \tau \sigma)\, \mathrm{d}\sigma, \tag{A 4b}$$

where v_s is a positive real chosen for our convenience in (A 6) below. In obtaining (A 4), we have cancelled the contributions from each Φ_n-integral from 0 to $\omega^{-n} v_s$ on the basis of the identity $\omega^{-1}\mathrm{Ai}(\omega^{-1}v) + \mathrm{Ai}(v) + \omega \mathrm{Ai}(\omega v) = 0$ (see Roberts 1967*b*, figure 3 and discussion below it). The idea is to evaluate the remaining integrals (A 4*b*) by the method of steepest descents. For $\tilde{\Phi}_1$, we make the change of variables $\sigma = \omega^{-1} v$, use the appropriate asymptotic form for Ai in the relevant sector on the complex plane (cf. Roberts 1967*b*, figure 2 in the $n = -1$ context) to obtain the asymptotic representation

$$\tilde{\Phi}_1 \sim \int_{v_s}^{v_s + \mathrm{i}\infty} \frac{\exp(g(v))}{\mathrm{i}\sqrt{4\pi}\,(v + \xi)^{1/4}}\, \mathrm{d}v \tag{A 5a}$$

https://doi.org/10.1017/S0022112001006711 Published online by Cambridge University Press

for $-\tau \gg 1$, where

$$g(v) = \tfrac{2}{3}\left[2v^{3/2} - (v+\xi)^{3/2}\right] + v\tau. \tag{A 5b}$$

Like Roberts (1967), we start the integration from the saddle point v_s, which solves

$$g'(v_s) = 2v_s^{1/2} - (v_s+\xi)^{1/2} + \tau = 0. \tag{A 6a}$$

For $\xi \ll \tau^2$, it determines

$$v_s^{1/2} \sim -\tau\left(1 + \frac{\xi}{2\tau^2}\right), \quad (v_s+\xi)^{1/2} \sim -\tau\left(1+\frac{\xi}{\tau^2}\right), \tag{A 6b}$$

from which we obtain

$$g(v_s) \sim \tfrac{1}{3}\tau^3 + \tau\xi. \tag{A 7a}$$

The steepest-descent integration off the saddle in the positive imaginary direction then determines

$$\tilde{\Phi}_1 \sim \tfrac{1}{2}\exp\left(\tfrac{1}{3}\tau^3 + \tau\xi\right). \tag{A 7b}$$

Then the sum $\tilde{\Phi}_{-1} + \tilde{\Phi}_1$ dominate the contributions to $\tilde{\Phi}$ and together with (A 1) yield the initial boundary layer form (5.9) for $-\tau\xi = O(1)$. This conclusion is important as it finally establishes our claim that (A 2) is the solution to our diffusion problem.

To obtain the large positive-τ behaviour we first evaluate the dominant contribution Φ_0, again using the large-argument asymptotic representation for Ai. It yields

$$\Phi_0 \sim \int_0^\infty \frac{\exp(f(\sigma))}{\sqrt{4\pi}\,(\sigma+\xi)^{1/4}}\,\mathrm{d}\sigma \tag{A 8a}$$

for $\tau \gg 1$, where

$$f(\sigma) = -\tfrac{2}{3}(\sigma+\xi)^{3/2} + \sigma\tau. \tag{A 8b}$$

The saddle point σ_s, which solves

$$f'(\sigma_s) = -(\sigma_s+\xi)^{1/2} + \tau = 0 \quad \text{is} \quad \sigma_s = \tau^2 - \xi \equiv -\rho. \tag{A 9a}$$

It determines

$$f(\sigma_s) \sim \tfrac{1}{3}\tau^3 - \tau\xi. \tag{A 9b}$$

For $\rho = O(\tau^{1/2})$, asymptotic evaluation in the neighbourhood of the saddle yields

$$\Phi \sim \tfrac{1}{2}\exp\left(\tfrac{1}{3}\tau^3 - \tau\xi\right)\operatorname{erfc}\left(\frac{\rho}{\sqrt{4\tau}}\right). \tag{A 10}$$

With (A 1a) this determines the leading-order approximation to the asymptotic solution (5.10).

To obtain the next-order term we consider Φ_1, which we evaluate using the large-argument expansion of $\mathrm{Ai}(\xi+\omega\sigma)$ alone. It gives

$$\Phi_1 \sim \int_0^\infty \frac{\mathrm{Ai}(\sigma)}{\mathrm{Ai}(\omega\sigma)}\,\frac{\exp(h(\sigma))}{\sqrt{4\pi}\,(\xi+\omega\sigma)^{1/4}}\,\mathrm{d}\sigma, \tag{A 11a}$$

where

$$h(\sigma) = -\tfrac{2}{3}(\xi+\omega\sigma)^{3/2} + \omega\sigma\tau. \tag{A 11b}$$

Since the ratio of the two Airy functions decays exponentially as $\sigma \uparrow \infty$, we expand (A 11b) on the basis that $\rho = O(\tau^{1/2})$, $\tau \gg 1$ and $\sigma = O(1)$. To that end, we write $\xi = \tau^2 + \rho$ and retain the first three terms in the binomial expansion of $[\tau^2 + (\rho+\omega\sigma)]^{3/2}$.

https://doi.org/10.1017/S0022112001006711 Published online by Cambridge University Press

It yields

$$h(\sigma) \sim \tfrac{1}{3}\tau^3 - \tau\xi - \frac{(\rho+\sigma\omega)^2}{4\tau}. \tag{A 12}$$

Here the terms proportional to σ are negligible, when $\sigma = O(1)$. In this way, we obtain the leading-order result

$$\Phi_1 \sim \frac{\delta_1}{\sqrt{4\pi\tau}} \exp\left(\tfrac{1}{3}\tau^3 - \tau\xi - \frac{\rho^2}{4\tau}\right), \quad \text{where} \quad \delta_n := \int_0^\infty \frac{\mathrm{Ai}(\sigma)}{\mathrm{Ai}(\omega^n\sigma)}\,\mathrm{d}\sigma, \tag{A 13a,b}$$

with $n = 1$.

Finally we note that, for $\rho = O(\tau^{1/2})$, $\tau \gg 1$, our proposed asymptotic solution (5.10) has the Taylor series expansion

$$\frac{1}{2}\,\mathrm{erfc}\left(\frac{\rho-\delta}{\sqrt{4\tau}}\right) \sim \frac{1}{2}\,\mathrm{erfc}\left(\frac{\rho}{\sqrt{4\tau}}\right) + \frac{\delta}{\sqrt{4\pi\tau}} \exp\left(-\frac{\rho^2}{4\tau}\right). \tag{A 14a}$$

This agrees with our results (A 10) and (A 13) when

$$\delta = \delta_{-1} + \delta_1, \tag{A 14b}$$

which with (A 13b) reduces to (5.11c).

REFERENCES

Abramowitz, M. & Stegun, I. A. 1964 *Handbook of Mathematical Functions*. Dover.

Dormy, E. 1997 Modélisation numérique de la dynamo terrestre. PhD thesis, IPG Paris.

Dormy, E., Cardin, P. & Jault, D. 1998 MHD flow in a slightly differentially rotating spherical shell, with conducting inner core, in a dipolar magnetic field. *Earth Planet. Sci. Lett.* **160**, 15–30.

Ferraro, V. C. A. 1937 Non-uniform rotation of the sun and its magnetic field. *Mon. Not. R. Astron. Soc.* **97**, 458–472.

Glatzmaier, G. A. & Roberts, P. H. 1995 A three-dimensional convective dynamo solution with rotating and finitely conducting inner core and mantle. *Phys. Earth Planet. Inter.* **91**, 63–75.

Hollerbach, R. 1994 Magnetohydrodynamic Ekman and Stewartson layers in a rotating spherical shell. *Proc. R. Soc. Lond.* A **444**, 333–346.

Hollerbach, R. 2000 Magnetohydrodynamical flows in spherical shells. In *Physics of Rotating Fluids* (ed. C. Egbers & G. Pfister), Lecture Notes in Physics, vol. 549, pp. 295–316. Springer (to appear).

Hollerbach, R. 2001 Super- and counter-rotating jets and vortices in strongly magnetic spherical Couette flow. In *Dynamo and Dynamics, A Mathematical Challenge* (ed. P. Chossat, D. Armbruster & I. Oprea). NATO Science Series II, vol. 26, pp. 189–197. Kluwer.

Hollerbach, R. & Skinner, S. 2001 Instabilities of magnetically induced shear layers and jets. *Proc. Roy. Soc. Lond.* A **457**, 785–802.

Kleeorin, N., Rogachevskii, I., Ruzmaikin, A., Soward, A. M. & Starchenko, S. 1997 Axisymmetric flow between differentially rotating spheres in a dipole magnetic field. *J. Fluid Mech.* **344**, 213–244.

Moore, D. W. & Saffman, P. G. 1969 The structure of free vertical shear layers in a rotating fluid and the motion produced by a slowly rising body. *Proc. R. Soc. Lond.* A **264**, 597–634.

Müller, U. & Bühler, L. 2001 *Magnetofluiddynamics in Channels and Containers*. Springer.

Proudman, I. 1956 The almost-rigid rotation of viscous fluid between concentric spheres. *J. Fluid Mech.* **1**, 505–516.

Roberts, P. H. 1967*a* *An Introduction to Magnetohydrodynamics*. Longmans, London.

Roberts, P. H. 1967*b* Singularities of Hartmann layers. *Proc. R. Soc. Lond.* A **300**, 94–107.

Roberts, P. H. 2000 Magnetohydrodnamics and the Earth's core: Selected works of Paul Roberts. In *The Fluid Mechanics of Astrophysics and Geophysics*, vol. 9 (ed. A. M. Soward). Gordon and Breach (to appear).

https://doi.org/10.1017/S0022112001006711 Published online by Cambridge University Press

STARCHENKO, S. V. 1997 Magnetohydrodynamics of a viscous spherical layer rotating in a strong potential field. *JETP* **85** (6), 1125–1137 (*Zh. Eksp. Teor. Fiz*. **112**, 2056–2078).

STARCHENKO, S. V. 1998*a* Magnetohydrodynamic flow between insulating shells rotating in strong potential field. *Phys. Fluids* **10**, 2412–2420.

STARCHENKO, S.V. 1998*b* Strong potential field influence on slightly differentially rotating spherical shells. *Studia Geoph. Geod*. **42**, 314–319.

STEWARTSON, K. 1966 On almost rigid rotation. Part 2. *J. Fluid Mech.* **26**, 131–144.

VIDALE, J. E., DODGE, D. A. & EARLE, P. S. 2000 Slow differential rotation of the Earth's inner core indicated by temporal changes in scattering. *Nature* **405**, 445–448.

WAECHTER, T. T. 1969 Steady magnetohydrodynamic flow in an insulating circular pipe. *Mathematica* **16**, 249–262.

https://doi.org/10.1017/S0022112001006711 Published online by Cambridge University Press